

THE EXCITATION AND METALLICITY OF GALACTIC H II REGIONS FROM *INFRARED SPACE OBSERVATORY* SWS OBSERVATIONS OF MID-INFRARED FINE-STRUCTURE LINES¹

URIEL GIVEON AND AMIEL STERNBERG

School of Physics and Astronomy and the Wise Observatory, Beverly and Raymond Sackler Faculty of Exact Sciences, Tel Aviv University, Tel Aviv 69978, Israel; giveon@wise.tau.ac.il, amiel@wise.tau.ac.il

DIETER LUTZ AND HELMUT FEUCHTGRUBER

Max-Planck-Institut für Extraterrestrische Physik, Giessenbachstrasse, 85748 Garching, Germany; lutz@mpe.mpg.de, fgb@mpe.mpg.de

AND

A. W. A. PAULDRACH

Institute for Astronomy and Astrophysics of Munich University, Scheinerstrasse 1, D-81679 Munich, Germany; uh10107@usm.uni-muenchen.de

Received 2001 May 16; accepted 2001 October 17

ABSTRACT

We present mid-infrared *Infrared Space Observatory* Short-Wavelength Spectrometer (*ISO*-SWS) observations of the fine-structure emissions lines [Ne II] 12.8 μm , [Ne III] 15.6 μm , [Ne III] 36.0 μm , [Ar II] 6.99 μm , [Ar III] 8.99 μm , [S III] 18.7 μm , [S III] 33.5 μm , and [S IV] 10.5 μm and the recombination lines Br α and Br β in a sample of 112 Galactic H II regions and 37 nearby extra-Galactic H II regions in the LMC, SMC, and M33. We selected our sources from archival *ISO*-SWS data as those showing prominent [Ne II] 12.8 μm or [Ne III] 15.6 μm emissions. The Galactic sources have a wide range in galactocentric distance ($0 \text{ kpc} \lesssim R_{\text{gal}} \lesssim 18 \text{ kpc}$), which enables us to study excitation and metallicity variations over large Galactic scales. We detect a steep rise in the [Ne III] 15.6 μm /[Ne II] 12.8 μm , [Ar III] 8.99 μm /[Ar II] 6.99 μm , and [S IV] 10.5 μm /[S III] 33.5 μm excitation ratios from the inner Galaxy outward, and a moderate decrease in metallicity, from $\sim 2 Z_{\odot}$ in the inner Galaxy to $\sim 1 Z_{\odot}$ in the outer disk. The extra-Galactic sources in our sample show low gas density, low metallicity, and high excitation. We find a good correlation between [Ne III] 15.6 μm /[Ne II] 12.8 μm and [Ar III] 8.99 μm /[Ar II] 6.99 μm excitation ratios in our sample. The observed correlation is well reproduced by theoretical nebular models that incorporate new-generation wind-driven non-LTE model stellar atmospheres for the photoionizing stars. In particular, the non-LTE atmospheres can account for the production of [Ne III] emission in the H II regions. We have computed self-consistent nebular and stellar atmosphere models for a range of metallicities ($0.5\text{--}2 Z_{\odot}$). We conclude that the increase in nebular excitation with galactocentric radius is due to an increase in stellar effective temperature (as opposed to a hardening of the stellar spectral energy distributions due to the metallicity gradient). We estimate an integrated [Ne III] 15.6 μm /[Ne II] 12.8 μm ratio for the Galaxy of 0.8, which puts it well inside the range of values for starburst galaxies. The good fit between observations and our models support the conclusion of Thornley and coworkers that the low [Ne III] 15.6 μm /[Ne II] 12.8 μm ratios observed in extra-Galactic sources are due to global aging effects.

Subject headings: galaxies: individual (M33) — Galaxy: abundances — Galaxy: stellar content — H II regions — Magellanic Clouds — stars: atmospheres

On-line material: machine-readable table

1. INTRODUCTION

Mid-infrared (IR) fine-structure emission lines are useful probes of the physical properties of H II regions and their associated ionizing sources. Unlike optical and UV emission lines, the fine-structure lines do not suffer as much from dust extinction, and the low energies of the fine-structure levels ($h\nu/k \sim 10^2\text{--}10^3 \text{ K}$) make the fine-structure lines relatively insensitive to the nebular electron temperature T_e ($\sim 10^4 \text{ K}$ in H II regions). Fine-structure line emissions from photoionized gas have been observed in a wide range of astrophysical sources (Genzel et al. 1998; Cox et al. 1999; Thornley et al. 2000). Their measured intensities have been shown to be strong, comparable to optical hydrogen recombination lines. The relative strengths of the fine-structure

emission lines may be used to probe the ionizing spectral energy distributions (SEDs) because different ionization stages are formed by significantly different photon energy ranges in the ionizing spectrum. For example, the [Ne III] 15.6 μm /[Ne II] 12.8 μm line ratio is sensitive to photons emitted at the $\gtrsim 3 \text{ ryd}$ region, while [Ar III] 8.99 μm /[Ar II] 6.99 μm probes the region $\gtrsim 2 \text{ ryd}$. Measuring these (and other) ratios can constrain the SEDs of the hot stars in H II regions (Thornley et al. 2000; Förster Schreiber et al. 2001a) or of the nonstellar sources in active galactic nuclei (Alexander et al. 1999, 2000).

The Short-Wavelength Spectrometer (SWS) on board the *Infrared Space Observatory* (*ISO*) made spectroscopic studies of Galactic and extra-Galactic sources possible across the entire mid-infrared (2.5–45 μm) spectral range (de Graauw et al. 1996; Kessler et al. 1996; Genzel & Cesarsky 2000). In this paper we have compiled SWS observations of fine-structure emission lines from Galactic and nearby extra-Galactic H II regions from the *ISO* data archive. The sources were selected as those in which the [Ne II] 12.8 μm

¹ Based on observations with *ISO*, an ESA project with instruments funded by ESA member states (especially the PI countries: France, Germany, the Netherlands, and the United Kingdom) with the participation of ISAS and NASA.

or [Ne III] 15.6 μm lines are present, eliminating target types other than H II regions. Since these objects are typically prominent sources of the diagnostically useful [Ar II] 6.99 μm , [Ar III] 8.99 μm , [S III] 18.7 μm , [S III] 33.5 μm , and [S IV] 10.5 μm fine-structure lines and the Br α and Br β recombination lines, we extracted these lines as well for sources in which they were observed.

In this paper we have several goals: First, we wish to reinvestigate the large-scale variations in elemental abundances and nebular excitation across the Galactic disk. The Galactic sources in our sample have a wide enough range in galactocentric distance ($0 \text{ kpc} \lesssim R_{\text{gal}} \lesssim 18 \text{ kpc}$) to enable us to study these variations. Such studies using *ISO* data have been presented by Cox et al. (1999) for a sample of 46 Galactic H II regions over a range of 0–25 kpc in galactocentric radius and showed that the excitation ratios [Ne III] 15.6 μm /[Ne II] 12.8 μm and [Ar III] 8.99 μm /[Ar II] 6.99 μm increase as a function of the galactocentric radius. They also showed that the argon and neon abundances, based on observations of [Ne II] 12.8 μm and [Ar II] 6.99 μm , decrease by a factor of 2 from the inner Galaxy outward (see also Roelfsema et al. 1999 and Martín-Hernández 2000). These results are consistent with the trends found in earlier studies of Galactic H II regions using ground-based and airborne observations (Simpson et al. 1995; Afflerbach, Churchwell, & Werner 1997). Here we present results for a larger source sample. Understanding the excitation gradient within our Galaxy may shed further light on excitation variations observed in external galaxies (e.g., Shields & Tinsley 1976 in M101; Henry & Howard 1995 in M33, M81, and M101; see also Shields 1990).

Second, we use the observations as templates for constraining the results of new-generation wind-driven (non-LTE) stellar atmosphere computations (Pauldrach, Hoffmann, & Lennon 2001). For example, a long-standing problem in Galactic H II region studies has been the failure of photoionization simulations employing old-generation static (LTE) atmospheres (Kurucz 1992) to reproduce the observed (high excitation) [Ne III] line emission (Baldwin et al. 1991; Simpson et al. 1995). We reinvestigate (and resolve) this issue here using non-LTE (NLTE) atmospheres. In our analysis we construct an [Ar III] 8.99 μm /[Ar II] 6.99 μm versus [Ne III] 15.6 μm /[Ne II] 12.8 μm diagnostic diagram as a measure of the nebular excitation. We fit the observed correlation between these two line ratios by constructing nebular simulations in which the photoionizing stellar SEDs are modeled using NLTE atmosphere computations. We compare with results obtained using the older LTE Kurucz atmospheres. We also explore the effects of metallicity variations by self-consistently varying the nebular and the stellar atmosphere abundances.

This paper is a part of a larger framework, whose aims are to study theoretical models of starburst regions as they are probed by IR spectroscopy (Kunze et al. 1996; Lutz et al. 1996; Rigopoulou et al. 1996; Sturm et al. 1997; Genzel et al. 1998; Thornley et al. 2000; Förster Schreiber et al. 2001a, 2001b). For example, Thornley et al. (2000) measured the [Ne III] 15.6 μm /[Ne II] 12.8 μm excitation ratio in extra-Galactic starburst sources and found it to be *low* compared to starburst models that incorporate the new-generation atmospheres. They concluded that this is evidence for global aging of the star-forming regions. Fine-structure emission lines have also been used to try to determine the primary energy source in the ultraluminous

infrared galaxies (ULIRGs; Lutz et al. 1996; Genzel et al. 1998; Rigopoulou et al. 1999). Understanding the properties of the SEDs of hot stars, as probed by Galactic H II regions, is crucial to the interpretation of the extra-Galactic observations.

2. OBSERVATIONS

2.1. Data Reduction and Source Selection

The *ISO* data archive contains several thousands of observations that were obtained with the 2.4–45 μm grating spectrometer SWS. We have identified potential H II regions in all observations taken in the full spectrum mode (SWS01) and the line spectroscopy mode (SWS02) during the *ISO* mission. An automatic procedure starting from the off-line processing Version 7 standard processed data (SPD) processed all these observations to the autoanalysis result (AAR) level. From every AAR, a spectral range of ± 30 resolution elements ($r = 2000$) around the [Ne II] 12.8 μm and [Ne III] 15.6 μm lines was cut out for further analysis. This processing was automated by a script which flat-fielded the individual detectors to their mean value, removed 3 σ outliers, and rebinned each line to a single-valued spectrum.

For the SWS01 data, a simple automatic removal of the SWS band 3 instrumental fringes was applied in this procedure when the continuum for the [Ne II] 12.8 and [Ne III] 15.6 μm lines exceeded 100 Jy. We then automatically fitted Gaussians to the rebinned spectral segments and measured line fluxes. A source was considered a candidate for in-depth processing if at least one of the two lines was apparently present at a level above $10^{-20} \text{ W cm}^{-2}$.

For the SWS02 data, the automatically produced single-valued spectral segments for each line were stored and later inspected visually for the presence of lines, which finally gave a list of observation number and target name for every clear detection of either [Ne II] 12.8 μm or [Ne III] 15.6 μm or both. Visual inspection was preferred here, since the defringing step in AOT02 observations is less robust, and a lot of faulty detections would occur otherwise.

Our selection procedure initially gave also objects of similar spectral characteristics (nearby galaxies, planetary nebulae, etc.) that were subsequently identified and excluded from further processing. All observations from the list of candidate H II regions were then reprocessed, and the line fluxes were measured. In Table 1 we list the specific emission lines included in our source sample, together with

TABLE 1
IR FINE-STRUCTURE LINES, WHICH WERE MEASURED IN THE SPECTRA
SELECTED FROM THE *ISO* ARCHIVE, WITH THEIR WAVELENGTHS,
IONIZATION POTENTIALS, AND CRITICAL DENSITIES

Line	Wavelength (μm)	Ionization Potential (eV)	Critical Density (cm^{-3})
Br α	4.05		
Br β	2.63		
[Ar II]	6.99	27.63	4.17×10^5
[Ar III] ...	8.99	40.74	2.60×10^5
[Ne II] ...	12.81	40.96	7.00×10^5
[Ne III] ...	15.56	63.45	2.68×10^5
[Ne III] ...	36.01	63.45	5.50×10^4
[S III]	18.71	34.79	2.22×10^4
[S III]	33.48	34.79	7.04×10^3
[S IV]	10.51	47.22	5.39×10^4

their ionization potentials, line wavelengths, and critical densities for electron impact collisions.

For the SWS01 data, this needed special care since a large fraction of the observations was taken in the faster speed options of the SWS01 mode. For these observations, the grating moved during integrations, causing curved integration ramps when passing a strong emission line. The automatic deglitching of the SWS data occasionally confused such curved ramps with jumps in the ramps that correspond to glitches caused by ionizing particle hits and thus might have affected emission line fluxes (§ 4.5 of *ISO Handbook Vol. 6, The Short Wavelength Spectrometer, SAI-2000-008/Dc, Version 1.1*).² All SWS01 data except for the slowest speed 4 were hence reprocessed twice from ERD level, once with standard OLP Version 8 calibration files and once with one calibration file changed to switch off the glitch recognition. In both cases, the data were processed to the AAR level, cleaned from outliers by iterative clipping, flat-fielded, and rebinned to a single-valued spectrum. The two versions were then plotted and inspected to determine whether the deglitching might have affected the real line in the standard processing, or whether a glitch might have been present in these data with glitch recognition switched off. This classification was in most cases possible on the basis of feature shape and widths. The line flux or limit was then measured in that version not affected by problems. In a few cases with both versions affected, generous upper limits were adopted. SWS01 speed 4 and SWS02 data were processed by default before measuring line fluxes by direct integration of the continuum-subtracted line or determining upper limits corresponding to a line of 3σ peak height and the proper width. For SWS01 observations, this was done for all lines in Table 1; for SWS02, only for those present in a particular observation. The uncertainty in the line fluxes is estimated to be $\sim 30\%$.

The final identification of individual objects—whether it is an H II region or a different kind of source (e.g., nearby galaxy, planetary nebula) that was missed by the first filtering, or whether there were multiple observations of the same object—is based on a literature survey, mainly using the SIMBAD astronomical database.³

A total of 149 SWS spectra were selected for the final sample. This includes almost all of the H II regions observed by *ISO-SWS*—112 Galactic H II regions, spanning galactocentric radii of 0 to ~ 18 kpc, 14 H II regions in the Large Magellanic Cloud (LMC), 4 in the Small Magellanic Cloud (SMC), and 19 in the nearby spiral galaxy M33. This sample is certainly heterogeneous since it is a collection of targets observed for different proposals and scientific reasons. These include detailed studies of well-known individual H II regions, more systematic surveys of compact H II regions originally selected on the basis of *IRAS-LRS* spectra and on the basis of *IRAS* sources located outside the solar circle, observations of the brightest H II regions in the LMC, SMC, and M33, and H II region observations targeted at specific issues of ISM physics rather than a per se characterization of the H II region observed. The selection criteria adopted by these proposals necessarily differed, and incomplete execution of planned observations during the *ISO* mission induces another (though uncritical) selection effect. Some observations represent integrated fluxes of rather

compact well-defined H II regions; others different parts of more complex regions, including pointings in the outskirts of resolved nebulae. However, the sample spans H II regions with a wide enough range of positions and excitation conditions to study both the stellar SEDs and Galactic metallicity and nebular excitation gradients.

Metallicity gradient analyses in our Galaxy should be little affected by possible selection biases in our sample, as long as there is efficient mixing at a given galactocentric radius. The situation is less clear for excitation analyses where competing selection biases are possible. Selection on compactness, for example, might prefer younger (harder) but also less luminous (softer) objects, with additional effects due to dust possible. Similarly, optical rather than infrared/radio selection might prefer more evolved (softer) but also more luminous (harder) and lower metallicity (harder) objects, all perhaps more likely to be optically visible. Since a large fraction of the targets in the *ISO* database is originally *IRAS* selected, such effects are likely not governing excitation analyses as a function of galactocentric radius in our sample.

2.1.1. Calculation of Galactocentric Radius

We obtained radial velocity measurements for most of the Galactic sources from the literature (see references in Tables 2 and 3). These velocities were determined using different methods and are based on various emission features (e.g., radio recombination lines; sub-millimeter molecular lines of CO, CS, and CI; maser emission). In some cases (DR 21, Gal 007.47+00.06), the given velocity value is the mean between different values obtained from the same method (i.e., several recombination lines).

We use the Rohlfs & Kreitschmann (1987) Galactic rotation curve to calculate the galactocentric distance of each source. Their rotation curve spans a range of 0.1–19.4 kpc in galactocentric radius. For the Sun we adopt a galactocentric distance $R_{\odot} = 8.5$ kpc and rotational velocity $\theta_{\odot} = 220$ km s⁻¹ (Honma & Sofue 1997). We have transformed the rotation curve of Rohlfs & Kreitschmann ($R_{\odot} = 7.9$ kpc and $\theta_{\odot} = 184$ km s⁻¹) using the more updated solar values of Honma & Sofue. Most of the Galactic sources lie very near the Galactic plane (typically, $b < 5^{\circ}$), so we assume that they lie in the Galactic plane ($b = 0$). (An exception is the Orion Nebula ($b = -19.4^{\circ}$), for which the following procedure was not applied.) For each source having a radial velocity v_{LOS} and a Galactic longitude l , we compute the quantity $W(R_{\text{gal}})$, where $v_{\text{LOS}} = W(R_{\text{gal}}) \sin l$ and

$$W(R_{\text{gal}}) = \left[\theta(R_{\text{gal}}) \left(\frac{R_{\odot}}{R_{\text{gal}}} \right) - \theta_{\odot} \right]. \quad (1)$$

Here, R_{gal} is the galactocentric radius and $\theta(R_{\text{gal}})$ is the rotational velocity at R_{gal} . Using a linear interpolation of the $W(R_{\text{gal}})$ curve from Honma & Sofue, we find the values of R_{gal} corresponding to the $W(R_{\text{gal}})$ of each source.

The kinematic distance (R_{kin} ; distance from the Sun) is calculated by inverting the formula

$$R_{\text{gal}}^2 = R_{\odot}^2 - 2R_{\text{kin}} R_{\odot} \cos l + R_{\text{kin}}^2. \quad (2)$$

For sources outside the solar circle, this gives a single solution, whereas inside the solar circle, one obtains two solutions. The choice of distance in this case is based on different methods discussed in the references. A distance ambiguity remains for only three sources, designated with asterisks in Table 2 (col. [8]).

² See http://www.iso.vilspa.esa.es/manuals/HANDBOOK/VI/sws_hb.

³ See <http://simbad.u-strasbg.fr>.

TABLE 2
GALACTIC H II REGIONS DATA

No.	Name	R.A. (2000.0) (3)	Decl. (2000.0) (4)	R_{kin} (5)	R_{gal} (6)	v_{Los} (7)	Ref. (8)	Br α (9)	Br β (10)	[Ar II] (11)	[Ar III] (12)	[Ne III] (13)	[Ne III] (14)	[Ne III] (15)	[S III] (16)	[S III] (17)	[S IV] (18)
1...	WB89 380	01 07 50.5	+65 21 23.1	11.3	17.6	-74.1	1	1.6	8.7	3.0	<0.6	5.2	2.6	1.0
2...	WB89 380	01 07 50.7	+65 21 21.7	11.3	17.6	-74.1	1	1.8	0.9	<2.6	1.5	9.6	3.6	<3.7	5.5	<6.6	<1.8
3...	WB89 399	01 45 39.6	+64 16 02.1	10.1	16.8	-82.2	18	<0.8	<1.3	<3.0	<1.7	3.3	<2.2	<1.8	<3.0	<3.3	<0.9
4...	W3 IRS 5	02 25 40.5	+62 05 51.3	4.2	11.8	-42.2	1	3.5	0.7	<18.0	<5.8	<32.0	<19.0	<27.0	16.6	36.1	3.3
5...	W3 IRS 2	02 25 44.6	+62 06 11.2	3.7	11.3	-38.8	1	63.3	22.0	25.1	101.0	348.0	882.0	252.0	570.0	585.0	228.0
6...	W3 IRS 2	02 25 44.6	+62 06 11.2	3.7	11.3	-38.8	1	63.5	20.1	25.1	119.0	348.0	888.0	192.0	414.0	546.0	259.0
7...	WB89 436	02 42 19.8	+62 53 51.8	8.9	16.1	-71.3	18	<0.4	<1.5	<1.3	<1.1	<2.5	<5.0	<3.7	<12.0	<30.0	<1.6
8...	S212	04 40 37.7	+50 27 22.0	7.9	16.1	-35.3	2	...	<0.2	<0.3	0.5	2.8	1.6	<0.2	2.8	6.7	0.6
9...	OR16	05 34 56.5	-05 17 01.8	0.5	8.9	...	2	0.6	0.5	3.0	...	7.2	<0.2	...	5.7	15.4	<0.2
10...	OR15	05 35 00.1	-05 17 06.5	0.5	8.9	...	2	0.5	<0.2	2.2	...	6.6	<0.4	...	4.1	13.3	<0.2
11...	ORIONPK1_1	05 35 13.7	-05 22 08.5	0.5	8.9	...	2	28.8	25.0	<4.3	...	299.0
12...	ORIONPK1_2	05 35 13.7	-05 22 08.5	0.5	8.9	...	2	27.8	24.6	24.2	69.4	279.0	278.0	<37.0	313.0	335.0	71.4
13...	ORIONIRC2	05 35 14.5	-05 22 29.8	0.5	8.9	...	2	60.7	34.5	<80.0	126.0	369.0	534.0	<300.0	505.0	231.0	200.0
14...	ORIONISW	05 35 14.7	-05 23 41.1	0.5	8.9	...	2	74.1	...	63.3	152.0	529.0	868.0	210.0	773.0	521.0	337.0
15...	ORIONPK2	05 35 15.8	-05 22 40.7	0.5	8.9	...	2	67.6	41.0	37.3	171.0	504.0	861.0	153.0	606.0	426.0	269.0
16...	ORIONBARD8	05 35 18.2	-05 24 39.9	0.5	8.9	...	2	41.7	22.3	26.7	113.0	324.0	408.0	98.4	429.0	609.0	136.0
17...	ORIONBARBRGA	05 35 19.3	-05 24 59.9	0.5	8.9	...	2	53.9	27.1	61.1	116.0	365.0	243.0	<57.0	494.0	534.0	49.4
18...	ORIONBARD5	05 35 19.8	-05 25 10.0	0.5	8.9	...	2	33.5	15.7	47.0	68.4	355.0	208.0	30.6	365.0	362.0	38.3
19...	ORIONBARD251	05 35 20.3	-05 25 19.1	0.5	8.9	...	2	14.6	9.1	17.2	29.2	125.0	67.9	21.0	174.0	362.0	15.6
20...	[WBH98] 06084-0611	06 10 50.2	-06 12 01.0	0.7	9.1	10.0	12	0.5	<1.1	1.7	<0.8	<1.5	<2.0	<7.1	<2.3	<7.5	<0.8
21...	GRS 281.56-02.48	09 58 02.7	-57 57 51.8	1.7	7.7	-27.5	5	3.0	1.0	16.8	<0.8	16.1	<1.0	<1.8	13.2	10.8	<0.5
22...	CAR_POL2	10 42 58.4	-59 32 54.3	2.5	7.9	...	7	<1.0	<2.7	2.5	<2.3	8.4	<6.6	<3.0	10.1	44.4	<1.6
23...	Caswell H2O 287.37-00.62	10 43 19.2	-59 34 19.3	2.5	7.9	-17.5	7	1.6	<2.7	6.1	4.3	22.8	18.0	7.2	29.8	132.0	2.8
24...	TRUMPLER14	10 43 23.1	-59 34 28.4	2.5	7.9	-20.0	4	6.4	4.4	3.7	11.3	34.0	54.8	18.3	68.7	245.0	9.6
25...	Gal 287.39-00.63	10 43 40.1	-59 35 44.2	2.5	7.7	-24.6	13	5.6	<3.6	<3.7	16.3	17.4	77.8	18.6	63.7	186.0	34.0
26...	Gal 289.88-00.79	11 00 59.8	-60 50 27.1	7.6	9.3	20.2	5	16.3	5.8	28.5	21.1	120.0	34.6	<5.9	149.0	150.0	14.6
27...	NGC 3603	11 15 07.1	-61 15 33.0	7.2	8.9	11.0	6	1.7	0.7	<0.8	4.1	13.0	34.5	12.6	25.4	77.0	15.7
28...	RAFGL 4127	11 16 33.8	-61 29 59.4	8.6	9.6	25.0	6	6.6	2.4	<2.3	12.3	21.4	94.8	21.6	72.9	154.0	75.7
29...	Gal 298.23-00.33	12 10 00.3	-62 49 56.5	10.8	10.1	31.0	6	65.9	26.7	7.5	102.0	124.0	802.0	174.0	382.0	362.0	557.0
30...	GRS 301.11+00.97	12 36 01.9	-61 51 03.9	4.4	7.2	-40.8	5	4.7	10.2	6.9	13.4	54.3	40.3	<20.0	77.3	209.0	11.5
31...	GRS 302.03-00.04	12 43 31.9	-62 55 11.4	5.7	7.3	-35.4	5	5.3	1.1	14.9	2.5	41.8	5.7	<3.0	22.6	20.8	<0.9
32...	RAFGL 4176	13 43 02.1	-62 08 52.0	5.3	6.4	-61.0	4	4.4	<3.8	8.4	<3.8	42.5	<8.2	<10.0	15.8	15.2	<3.3
33...	RAFGL 4972S	15 00 36.6	-58 58 15.8	11.0	7.3	-29.0	6	<0.8	<2.6	<1.6	<1.7	8.3	7.3	<9.9	6.7	29.4	<1.6
34...	GRS 321.71+01.16	15 13 50.2	-56 24 45.9	10.8	6.7	-41.3	5	3.9	<0.8	11.3	1.8	27.7	2.9	<2.9	26.0	83.0	<1.4
35...	GRS 326.44+00.91	15 42 17.2	-53 58 31.5	2.5	6.5	-41.0	5	26.4	10.1	73.6	53.6	289.0	95.2	16.6	254.0	312.0	25.5
36...	[WBH98] 15408-5356	15 44 42.8	-54 05 55.8	2.4	6.6	-38.8	5	29.7	11.0	77.1	59.7	394.0	294.0	60.3	441.0	512.0	53.4
37...	G327.3-0.5	15 53 05.9	-54 35 21.1	2.8	6.3	-45.0	5	28.7	11.8	134.0	47.3	444.0	190.0	44.4	497.0	854.0	27.5
38...	GRS 328.30+00.43	15 54 05.1	-53 11 36.4	8.9	4.8	-91.7	5	14.7	2.3	41.8	8.4	100.0	29.2	<20.0	48.8	94.9	2.4
39...	[WBH98] 15567-5236	16 00 32.9	-52 44 45.3	7.3	4.3	-107.1	5	25.7	6.8	55.8	17.8	160.0	64.2	<20.0	40.4	<36.0	6.4
40...	G331.28-0.19	16 11 26.6	-51 41 56.6	5.3	4.6	-87.7	5*	<0.9	<2.7	<2.8	<1.3	11.0	4.6	<6.4	11.0	104.0	<2.0
41...	[WBH98] 16172-5028	16 21 00.4	-50 35 21.1	3.5	5.6	-51.2	5	12.7	2.8	70.3	12.5	166.0	43.9	9.5	136.0	340.0	4.8
42...	G333.13-0.43	16 21 02.7	-50 35 58.1	3.8	5.4	-57.6	9	4.4	<2.5	10.8	8.0	79.4	44.6	11.7	100.0	262.0	12.0
43...	Gal 337.9-00.5	16 41 07.8	-47 07 32.7	3.0	5.8	-38.0	15	15.2	7.1	42.8	29.5	232.0	139.0	29.7	255.0	516.0	30.0
44...	[WBH98] 17059-4132	17 09 31.2	-41 35 55.5	2.3	6.3	-20.9	5	17.7	4.4	126.0	25.4	388.0	105.0	<20.0	398.0	574.0	6.7
45...	[WBH98] 17160-3707	17 19 26.1	-37 10 53.8	10.7	2.8	-69.5	5	3.0	<1.4	15.5	1.5	38.2	<10.0	<5.5	25.1	131.0	<1.6
46...	NGC 6334_A	17 20 19.3	-35 54 54.9	1.0	7.5	-5.0	5	5.0	<2.9	32.3	2.8	98.5	17.2	9.8	44.3	171.0	6.8

TABLE 2—Continued

No.	Name	R.A. (2000.0)	Decl. (2000.0)	R_{kin}	R_{gal}	v_{los}	Ref.	Brz	Br β	[Ar II]	[Ar III]	[Ne II]	[Ne III]	[Ne III]	[S III]	[S III]	[S IV]
(1)	(2)	(3)	(4)	(5)	(6)	(7)	(8)	(9)	(10)	(11)	(12)	(13)	(14)	(15)	(16)	(17)	(18)
47...	NGC 6334 IRS 1	17 20 52.1	-35 47 02.4	1.3	7.2	-7.0	5	10.0	<3.0	57.0	<3.0	155.0	<11.0	<28.0	15.4	13.8	<3.2
48...	NGC 6334-ISWS	17 20 53.4	-35 47 01.4	1.3	7.2	-7.0	5	14.5	2.9	87.7	2.1	194.0	2.9	<28.0	30.6	<40.0	<1.9
49...	NGC 63571	17 24 40.3	-34 10 20.1	0.8	7.7	-3.0	3	11.5	3.3	10.3	34.8	95.5	118.0	32.8	251.0	560.0	51.0
50...	Gal 351.47 - 00.46	17 25 31.7	-36 21 53.5	3.5	5.1	-22.3	5	5.5	<2.0	28.0	5.8	84.4	<4.7	<8.5	63.1	170.0	1.5
51...	NGC 6357IIIB	17 25 34.9	-34 22 36.1	1.1	7.4	-4.5	3	4.0	<4.3	<20.0	11.6	59.5	33.7	9.2	86.4	240.0	9.6
52...	Gal 351.20 - 00.05	17 31 17.1	-33 52 49.3	5.4	3.2	-32.3	5	2.7	<0.7	21.0	<1.6	49.7	<3.9	<2.9	30.3	149.0	<1.0
53...	Gal 359.43 - 00.09	17 44 35.6	-29 27 29.3	8.2	0.3	-60.0	6	2.4	<3.0	25.6	<1.0	45.5	<3.9	<7.8	14.7	120.0	<1.4
54...	Gal 359.43 - 00.09	17 44 35.9	-29 27 54.3	8.2	0.3	-60.0	6	2.4	...	20.0	0.6	48.9	2.4	0.8
55...	GCRINGSW	17 45 38.6	-29 01 05.7	8.5	0.0	...	1	8.1	2.1	75.2	<0.2	113.0	6.0	2.0	20.2	137.0	<0.3
56...	RAFGL 2003	17 45 39.1	-29 00 22.6	8.5	0.0	...	1	46.6	12.9	422.0	9.4	947.0	48.1	15.0	149.0	483.0	5.8
57...	GAL CENTER IRS 1W	17 45 40.0	-29 00 28.6	8.5	0.0	...	1	61.7	16.4	436.0	8.1	801.0	45.1	18.5	151.0	465.0	<2.0
58...	GAL CENTER IRS 24	17 45 41.8	-28 59 50.5	8.5	0.0	...	1	2.3	1.3	37.6	<0.3	66.8	4.6	2.2	8.4	67.6	<0.2
59...	ARCHFILNW	17 45 43.9	-28 48 38.1	8.5	0.0	...	10	4.0	1.0	28.9	3.1	80.9	3.1	<1.2	53.9	292.0	0.4
60...	ARCHFILSW	17 45 45.1	-28 50 19.0	8.5	0.0	...	10	5.5	1.4	44.0	2.9	104.0	4.3	<2.1	64.9	362.0	0.3
61...	ARCHCLUSTER	17 45 50.5	-28 49 28.1	8.5	0.0	...	10	2.6	0.5	11.1	0.4	26.7	1.7	<0.5	14.4	113.0	0.2
62...	G018.2	17 46 14.2	-28 47 47.1	8.2	0.3	24.5	17	5.1	<2.6	31.7	<2.9	52.3	13.1	<9.1	34.9	200.0	<2.4
63...	GCS 31	17 46 14.8	-28 49 33.1	8.0	0.5	...	10	3.2	<1.5	6.1	<1.5	13.0	<3.0	<2.5	5.4	34.7	<1.2
64...	Pistol Star	17 46 15.2	-28 50 03.1	8.0	0.5	...	10	7.1	2.5	25.4	1.4	51.0	22.3	5.9	32.2	89.6	1.3
65...	G0.18 - 0.04	17 46 15.4	-28 48 07.0	8.2	0.3	24.5	17	3.0	...	26.6	0.6	47.8	9.1	2.8
66...	GCS 4	17 46 15.7	-28 49 46.1	8.0	0.5	...	10	4.1	1.5	19.9	<1.7	40.4	14.4	4.6	26.3	68.8	<1.1
67...	GPSR5_099 - 0.167	17 46 31.4	-28 55 48.8	8.3	0.2	16.0	5	1.0	<0.9	7.6	<0.7	10.4	1.7	<1.7	6.4	49.2	<0.8
68...	RGR D H II	17 48 41.5	-28 01 38.3	10.0	1.5	-15.3	8	18.8	5.6	53.9	27.7	182.0	80.3	14.0	201.0	297.0	16.8
69...	RAFGL 2046	18 00 32.1	-24 04 03.4	2.4	6.1	9.3	5	2.5	<2.5	18.4	<1.7	27.5	7.4	<8.5	11.4	44.3	<2.5
70...	Gal 007.47 + 00.06	18 02 13.2	-22 27 59.3	6.3	2.4	-14.0	16	1.9	<1.7	<1.7	<1.3	12.5	29.4	11.3	9.9	44.9	<2.4
71...	[L89b] 9.615 + 00.198	18 06 13.9	-20 31 43.7	0.9	7.6	5.0	5	8.6	1.9	48.1	5.8	120.0	19.1	<12.0	72.8	123.0	<1.0
72...	RAFGL 2094	18 14 35.2	-16 45 20.6	4.4	4.4	49.2	5	11.1	3.4	64.6	<1.3	<4.0	<4.2	7.4	138.0	233.0	1.7
73...	M17 IRAMPOS8	18 20 19.3	-16 13 01.5	1.8	6.8	16.8	11	<0.8	<4.8	<1.3	<2.0	6.3	8.6	<5.0	4.0	18.0	<1.4
74...	M17 IRAMPOS7	18 20 20.7	-16 12 51.4	1.8	6.8	16.8	11	0.3	<1.5	<1.8	<2.0	6.3	8.6	<6.0	15.7	28.5	1.0
75...	M17 IRAMPOS6_1	18 20 22.1	-16 12 41.3	1.8	6.8	16.8	11	1.5	<1.5	<2.5	1.9	14.5	20.7	5.5	28.1	86.3	2.9
76...	M17 IRAMPOS6_2	18 20 22.1	-16 12 41.3	1.8	6.8	16.8	11	1.2	0.6	2.5	2.3	16.9	13.9	7.6	19.7	9.5	2.4
77...	M17 IRAMPOS5	18 20 23.4	-16 12 31.2	1.8	6.8	16.8	11	7.3	2.3	7.8	14.5	66.0	84.2	29.9	147.0	313.0	11.1
78...	M17 IRAMPOS4	18 20 24.8	-16 12 21.1	1.8	6.8	16.8	11	28.5	11.6	20.1	63.3	229.0	388.0	114.0	507.0	890.0	78.3
79...	M17 IRAMPOS3	18 20 26.2	-16 12 10.1	1.8	6.8	16.8	11	44.6	12.9	18.9	99.3	278.0	782.0	310.0	682.0	1810.0	235.0
80...	M17 IRAMPOS2	18 20 27.6	-16 12 00.9	1.8	6.8	16.8	11	49.8	18.5	8.5	126.0	208.0	1040.0	262.0	627.0	1350.0	482.0
81...	M17 IRAMPOS1	18 20 28.1	-16 11 50.8	1.8	6.8	16.8	11	22.2	9.0	10.7	60.8	121.0	483.0	103.0	391.0	704.0	269.0
82...	M17_3N	18 20 32.8	-16 01 42.5	1.5	7.0	13.9	11	4.8	<1.8	7.4	4.9	36.7	8.0	5.7	39.7	90.7	5.4
83...	M17_3NOFF	18 20 46.9	-16 03 45.5	1.7	6.8	15.8	11	<1.3	<2.9	<2.8	<1.8	5.9	<2.1	<2.5	6.8	26.3	<2.9
84...	RAFGL 7009S	18 34 20.6	-05 59 45.2	12.3	6.0	41.4	5*	<0.5	<0.8	<1.4	<0.7	<2.0	<1.9	<3.0	<1.8	<3.8	<1.2
85...	[WBH98] 18317 - 0757	18 34 24.9	-07 54 47.9	4.9	4.5	79.3	5	18.8	6.2	105.0	17.4	356.0	23.8	<7.4	260.0	261.0	2.9
86...	RAFGL 2245	18 46 03.1	-02 39 20.5	8.8	4.5	97.4	5	13.9	21.1	217.0	96.8	468.0	229.0	35.1	357.0	313.0	39.0
87...	IRAS 18441 - 0134	18 46 44.3	-01 30 54.6	4.9	5.0	80.8	14*	<0.9	<2.2	<2.2	<1.2	<3.0	<2.5	<2.9	<2.9	<3.9	<1.4
88...	[WBH98] 18469 - 0132	18 49 32.1	-01 29 03.6	5.3	4.8	87.7	5	1.8	<1.5	9.0	2.0	21.1	6.2	<5.2	25.0	80.1	<1.9
89...	RAFGL 5536	18 50 30.8	+00 01 59.4	13.3	7.7	15.0	5	5.0	<2.1	8.5	<2.3	53.6	28.9	10.2	23.2	25.6	<1.8
90...	Gal 033.91 + 00.11	18 52 50.2	+00 55 27.6	7.1	4.5	107.5	5	8.8	2.3	29.5	8.0	66.3	36.2	<9.5	59.9	86.6	5.1
91...	G045.066 + 0.138	19 13 22.0	+10 50 53.4	8.0	6.3	57.8	14	5.5	<2.5	8.1	<1.3	17.4	<7.7	<2.0	<17.0	<17.0	<1.2
92...	Gal 045.45 + 00.06	19 14 21.7	+11 09 13.6	7.9	6.3	58.0	5	12.0	3.0	17.2	19.0	127.0	131.0	24.3	119.0	228.0	19.8
93...	Gal 049.20 - 00.35	19 23 02.5	+14 16 40.6	5.6	6.2	65.4	5	6.4	<1.5	10.5	10.4	51.9	55.3	13.5	76.6	240.0	12.1
94...	W51 IRS 2	19 23 39.9	+14 31 06.1	8.9	7.3	33.0	4	77.4	22.4	52.4	92.2	506.0	983.0	108.0	337.0	236.0	137.0

TABLE 2—Continued

No. (1)	Name (2)	R.A. (2000.0) (3)	Decl. (2000.0) (4)	R_{kin} (5)	R_{gal} (6)	v_{LOS} (7)	Ref. (8)	Br α (9)	Br β (10)	[Ar II] (11)	[Ar III] (12)	[Ne II] (13)	[Ne III] (14)	[Ne III] (15)	[S III] (16)	[S III] (17)	[S IV] (18)
95 ...	[BE83] IR 070.29+01.60	20 01 45.5	+33 32 43.6	8.1	9.6	-25.2	5	43.1	14.8	24.5	29.2	140.0	297.0	<29.0	74.2	26.3	31.8
96 ...	[BE83] IR 070.29+01.60	20 01 45.7	+33 32 43.3	8.1	9.6	-25.2	5	46.7	15.6	20.3	26.2	111.0	256.0	19.2	78.8	53.3	25.8
97 ...	OH 78.12 + 3.63	20 14 25.1	+41 13 31.6	3.9	8.6	-3.8	5	<0.6	<1.3	<2.9	<0.7	<4.4	<3.9	<6.4	<2.4	<5.6	<1.5
98 ...	S106 PDR	20 27 25.7	+37 22 43.9	0.6	8.4	3.1	16	221.0	28.7
99 ...	S106 IRS 4	20 27 26.7	+37 22 47.9	0.6	8.4	3.1	16	41.4	14.7	89.9	26.8	305.0	37.9	<24.0	169.0	152.0	10.3
100 ...	S106 H2	20 27 27.1	+37 22 39.1	0.6	8.4	3.1	16	222.0	28.7
101 ...	Gal 081.68+00.54 (DR 21)	20 39 00.9	+42 19 41.9	2.2	8.5	0.4	1	7.5	2.3	25.9	2.4	47.2	<30.0	<18.0	22.1	42.3	<2.5
102 ...	Gal 081.68+00.54 (DR 21)	20 39 08.8	+42 19 53.4	2.2	8.5	0.4	1	<0.1	<1.5	<1.4	<0.8	<3.1	<3.1	<3.3	<5.6	6.2	<1.7
103 ...	S127	21 28 40.2	+54 36 29.4	15.3	18.3	-92.1	18	1.3	...	7.4	...	<0.6	6.4	12.8	0.2
104 ...	S127	21 28 40.2	+54 36 29.4	15.3	18.3	-92.1	18	1.5	...	7.5	...	<1.0	5.9	10.4	0.1
105 ...	S127	21 28 41.9	+54 36 51.5	15.3	18.3	-92.1	18	<0.5	<1.6	<2.4	<3.0	6.0	<2.6	<3.0	<4.6	11.6	<1.0
106 ...	S127	21 28 43.2	+54 37 27.1	15.3	18.3	-92.1	18	1.1	6.0	3.2	0.4	5.3	16.0	0.7
107 ...	S128 A	21 32 10.7	+55 52 45.1	9.4	13.5	-71.1	5	2.5	2.1	<1.6	3.1	18.8	10.3	<1.8	21.0	36.2	4.0
108 ...	S140	22 19 12.0	+63 18 06.4	0.8	8.8	-8.5	2	...	<0.1	0.3
109 ...	S138	22 32 45.9	+58 28 20.1	5.6	11.4	-52.1	5	6.0	3.5	16.2	4.3	43.1	<4.7	<9.5	44.0	40.9	1.1
110 ...	S138	22 32 45.9	+58 28 22.0	5.6	11.4	-52.1	5	5.4	<4.2	13.5	2.9	34.2	<2.2	<5.3	32.9	34.9	<1.3
111 ...	S156 A	23 05 10.6	+60 14 40.6	5.4	11.5	-52.1	5	15.5	6.7	17.0	26.9	133.0	22.5	<6.5	170.0	154.0	11.8
112 ...	S159	23 15 31.4	+61 07 08.5	5.9	12.0	-56.3	5	16.4	13.0	52.8	10.8	122.0	<12.0	<24.0	101.0	46.1	1.9

NOTES.—Col. (1): Source identification number in the sample. These numbers also appear as source identifications in the various figures. Col. (2): Source name. Cols. (3)–(4): Position (J2000.0) of the *ISO* aperture in right ascension and declination. Units of right ascension are hours, minutes, and seconds, and units of declination are degrees, arcminutes, and arcseconds. Col. (5): Kinematic distance (distance from the Sun) in kiloparsecs. Col. (6): Galactocentric radius (see § 2.1.1) in kiloparsecs. Col. (7): Source radial velocity in km s^{-1} . Col. (8): Acronym for the distance/radial velocity reference. The literature references are given in Table 3. Asterisks in col. (8) mean that there is no unique R_{kin} . Cols. (9)–(18): *ISO*-SWS fluxes for the lines listed in Table 1. The fluxes are in units of $10^{-19} \text{ W cm}^{-2}$. The error in the flux measurement is $\sim 30\%$. Table 2 is also available in machine-readable form in the electronic edition of the *Astrophysical Journal*.

TABLE 3
ABBREVIATION FOR THE REFERENCES OF TABLE 2

1. Afflerbach et al. 1996	10. Lang et al. 1999
2. Blitz, Fich, & Stark 1982	11. Lockman 1989
3. Brand et al. 1984	12. Shepherd & Churchwell 1996
4. Braz & Epchtein 1983	13. Slysh et al. 1994
5. Bronfman, Nyman, & May 1996	14. Szymczak, Hrynek, & Kus 2000
6. Caswell & Haynes 1987	15. Walsh et al. 1997
7. Caswell et al. 1989	16. Wink, Altenhoff, & Mezger 1982
8. Churchwell, Walmsley, & Cesaroni 1990	17. Wink, Wilson, & Bieging 1983
9. Huang et al. 1999	18. Wouterloot & Brand 1989

2.1.2. The Sources Data

Table 2 lists the data collected from the literature on the Galactic sources. In several cases, where observations of different parts of spatially resolved and complex regions were available, we summed the multiply observed intensities across the regions to a single value for each line. These observations are listed in Table 4. Table 5 lists the data for sources in the LMC and SMC. In Table 6 we list the data for sources in M33. In this table we also list the angular distance of each source from the center of M33.

A few studies of individual sources in our sample have been presented in the literature. For these sources our fluxes are in good agreement with the previously published fluxes. For example, in Orion IRC2 van Dishoeck et al. (1998) give fluxes for all of our lines (except for Br β) that are similar to the fluxes of our source 13. Similarly, van den Ancker, Tielens, & Wesselius (2000) published fluxes for the [Ne II] 12.8 μm , [Ne III] 15.6 μm , [S III] 18.7 μm , [S III] 33.5 μm , and [S IV] 10.5 μm fine-structure lines of S106 IR, which are comparable to those of our S106 IRS 4 (source 99). Rosenthal, Bertoldi, & Drapatz (2000) published fine-structure fluxes for all of the lines that we use in this paper for the Orion H₂ emission peak nebula (our sources 11 and 12). Rodríguez-Fernández, Martín-Pintado, & de Vicente (2001) give fluxes of several sources in the Galactic center from which six sources are included in our sample (62–67). They measured [Ne II] 12.8 μm , [Ne III] 15.6 μm , [S III] 18.7 μm , and [S III] 33.5 μm .

3. RESULTS

3.1. Excitation

We use the line ratios [Ne III] 15.6 μm /[Ne II] 12.8 μm , [Ar III] 8.99 μm /[Ar II] 6.99 μm , and [S IV] 10.5 μm /[S III] 33.5 μm to quantify the source excitation. In Figure 1 we show histograms of the observed [Ne III] 15.6 μm /[Ne II] 12.8 μm ratio (not corrected for extinction) for the groups of sources in our sample—the Milky Way, the LMC, the SMC, and M33, and for comparison, the sample of extra-Galactic sources as measured by Thornley et al. (2000). Filled bars designate sources whose ratios are uncertain. For the Milky Way and the starburst sample, these are all upper limits; for the LMC and SMC they are lower limits; whereas in M33 both cases are mixed together. It appears that the excitation distribution of Galactic H II regions is quite different from the distribution in the LMC, SMC, and M33, with smaller excitation in the Milky Way on average.

We can use our observations of Galactic H II regions to estimate an integrated value of the [Ne III] 15.6 μm /[Ne II] 12.8 μm ratio for our Galaxy that can be compared to the starburst galaxies. This is necessarily approximate since the sample drawn from the *ISO* archive is not an unbiased representation of the nebular luminosity of the Galaxy. The integrated ratio (not corrected for extinction) equals 0.8, with a dereddened value (see § 3.2) of 0.7. The corresponding median values are 0.41 and 0.36. These admittedly approximate values (shown as vertical lines overplotted on the Galactic and extra-Galactic histograms in Fig. 1) put our Galaxy well inside the range of [Ne III] 15.6 μm /[Ne II] 12.8 μm values for much more active starburst galaxies observed by Thornley et al. (2000), and even above its median.

In Figure 2 we plot the three excitation ratios mentioned above versus galactocentric radius for the Galactic sources. The data points are represented by the source identification numbers, as listed in Table 2. The displayed ratios have been corrected for extinction (§ 3.2). In this figure and the figures that follow, we designate limits on the given quantities by small arrows. Large arrows designate lower limits on the extinction correction.

Figure 2 shows a clear rise in the excitation toward the outer Galaxy. We have fitted power-law curves to the data in the range $2\text{kpc} \leq R_{\text{gal}} \leq 11\text{kpc}$. The fitted gradients are

$$\log \frac{[\text{Ne III}]15.6\mu\text{m}}{[\text{Ne II}]12.8\mu\text{m}} = 0.14(\pm 0.05)R_{\text{gal}} - 1.4(\pm 0.3), \quad (3)$$

$$\log \frac{[\text{Ar III}]8.99\mu\text{m}}{[\text{Ar II}]6.99\mu\text{m}} = 0.15(\pm 0.05)R_{\text{gal}} - 0.8(\pm 0.4), \quad (4)$$

and

$$\log \frac{[\text{S IV}]10.5\mu\text{m}}{[\text{S III}]33.5\mu\text{m}} = 0.19(\pm 0.04)R_{\text{gal}} - 1.9(\pm 0.3). \quad (5)$$

The observed excitation gradients are similar to those found in earlier studies of Galactic H II regions (Simpson et al. 1995; Afflerbach et al. 1997; Cox et al. 1999). We note that the [Ne III] 15.6 μm /[Ne II] 12.8 μm and [Ar III] 8.99 μm /[Ar II] 6.99 μm gradients are quite similar. This is an

TABLE 4
COMPLEX REGIONS, WHOSE INTENSITIES WERE SUMMED UP

Object	Observations (from Table 2)
Arches Cluster	59–61
Carina Nebula	22–25
IRAS 17431–2846	62, 65
IRAS 16172–5134	41, 42
IRAS 17424–2859 (Sagittarius A IRS 24)...	55–58
IRAS 17430–2848 (Pistol star).....	63, 64, 66
Omega Nebula (M17)	73–81
NGC 6334.....	47, 48
Orion Nebula (M42)	9–19
Gal 359.43–00.09	53, 54

TABLE 5
MAGELLANIC CLOUDS H II REGIONS DATA

No. (1)	Name (2)	R.A. (2000.0) (3)	Decl. (2000.0) (4)	Br α (5)	Br β (6)	[Ar II] 6.9 (7)	[Ar III] 8.9 (8)	[Ne II] 12.8 (9)	[Ne III] 15.6 (10)	[Ne III] 36.0 (11)	[S III] 18.7 (12)	[S III] 33.5 (13)	[S IV] 10.5 (14)
LMC													
113...	30DOR-R136/	05 38 42.6	-69 06 02.5	2.2	1.3	52	27.0
114...	30DORADUS #2/	05 38 35.4	-69 05 41.2	5.2	2.5	<0.7	7.5	9.0	64.7	12.5	34.7	98.5	44.0
115...	30DORADUS #4_1/	05 38 54.2	-69 05 15.3	2.8	1.3	0.3	4.9	6.7	37.1	8.7	22.7	76.4	17.9
116...	30DORADUS #4_2/	05 38 54.2	-69 05 15.3	2.3	<1.3	<1.8	4.9	10.7	36.0	12.5	24.4	71.9	1.9
117...	30DORH2/	05 38 44.5	-69 04 57.8	152	109.0
118...	N11A/	04 57 16.2	-66 23 18.4	0.3	0.6	<0.4	1.2	2.3	5.1	0.5	4.1	6.3	2.4
119...	N159-5/	05 40 02.4	-69 44 33.4	1.2	0.5	0.5	2.0	6.0	17.5	2.2	8.1	21.1	5.1
120...	N160A-IR/	05 39 43.7	-69 38 30.4	3.7	2.5	<1.3	5.8	16.4	46.1	5.9	21.9	47.6	15.8
121...	N160A1/	05 39 43.3	-69 38 51.4	4.7	2.4	0.5	7.2	13.0	51.0	7.3	30.2	64.8	25.6
122...	N160A2/	05 39 46.1	-69 38 36.6	5.4	2.8	1.3	7.4	13.9	38.0	5.6	26.5	49.4	16.4
123...	N160A3/	05 39 43.7	-69 38 30.4	3.7	1.8	1.3	5.1	12.7	32.0	3.7	18.6	40.7	11.5
124...	N4A/	04 52 08.4	-66 55 23.4	1.7	1.0	1.0	2.4	5.0	13.7	2.5	9.4	21.7	6.7
125...	N79A/	04 51 47.4	-69 23 47.7	<0.1	<0.1	<0.4	<0.2	<0.5	0.9	<0.2	0.6	3.3	0.2
126...	N83B/	04 54 25.2	-69 10 59.8	1.0	0.5	<0.4	1.0	2.3	3.5	0.5	3.3	5.5	1.9
SMC													
127...	N66/	00 59 03.7	-72 10 39.9	<0.2	0.1	<0.6	<0.4	<0.3	1.3	<0.5	0.7	1.8	1.2
128...	N81/	01 09 13.6	-73 11 41.1	<0.6	0.3	<0.3	0.4	0.2	2.7	0.4	1.6	2.4	1.4
129...	N88_1/	01 24 08.0	-73 09 02.5	1.0	0.8	<0.6	0.8	<0.4	3.0	0.5	1.1	0.9	4.9
130...	N88_2/	01 24 08.1	-73 09 03.1	1.5	<2.9	<1.5	<1.2	<1.6	6.7	<3.5	<3.3	<3.5	6.8

NOTES.—Units of right ascension are hours, minutes, and seconds, and units of declination are degrees, arcminutes, and arcseconds. The fluxes are in units of $10^{-19} \text{ W cm}^{-2}$.

TABLE 6
M33 CLOUDS H II REGIONS DATA

No. (1)	Name (2)	R.A. (2000.0) (3)	Decl. (2000.0) (4)	R_{M33} (5)	Br α (6)	Br β (7)	[Ar II] 6.9 (8)	[Ar III] 8.9 (9)	[Ne II] 12.8 (10)	[Ne III] 15.6 (11)	[Ne III] 36.0 (12)	[S III] 18.7 (13)	[S III] 33.5 (14)	[S IV] 10.5 (15)
131...	M33 C004/	01 33 59.3	+30 35 49.2	3 21	...	<0.2	0.5	<0.6
132...	M33 C027/	01 33 45.5	+30 36 51.1	2 22	...	<0.2	0.2	<0.2
133...	M33 C041/	01 33 35.5	+30 39 30.5	2 22	...	<0.1	0.2	<0.5
134...	M33 C045/	01 33 28.8	+30 40 24.7	3 45	...	<0.2	0.5	1.1
135...	M33 C049/	01 33 33.9	+30 41 28.3	3 45	...	<0.2	1.2	0.8
136...	M33 C079/	01 34 00.2	+30 40 48.6	1 41	...	<0.2	0.8	0.6
137...	M33 C088W/	01 34 15.5	+30 37 12.4	3 21	...	<0.2	0.2	0.3
138...	M33 C095/	01 34 10.9	+30 36 18.1	3 45	...	<0.2	0.3	<0.4
139...	M33 C214/	01 33 29.1	+30 31 46.8	7 52	...	<0.2	0.4	<0.2
140...	M33 C251/	01 33 36.6	+30 20 13.4	18 55	...	<0.2	<0.2	0.3
141...	M33 C280/	01 32 45.2	+30 38 53.7	8 48	...	<0.2	<0.2	0.6
142...	M33 C302/	01 34 06.9	+30 47 25.9	8 38	...	<0.2	0.6	<0.5
143...	M33 C623_1/	01 33 16.5	+30 52 49.1	14 38	...	<0.2	0.3	0.9
144...	M33 C623_2/	01 33 16.3	+30 52 47.8	14 38	0.1	<0.1	<0.2	0.1	<0.4	0.7	<0.7	0.3	<0.3	0.4
145...	M33 C638E/	01 33 16.3	+30 56 43.8	18 23	...	<0.2	<0.2	0.3
146...	M33 C680B/	01 34 33.5	+30 46 50.5	9 21	...	<0.3	1.8	1.7
147...	M33 C680C/	01 34 32.1	+30 46 59.9	9 21	...	<0.2	2.5	2.7
148...	M33 C691/	01 34 16.4	+30 51 55.1	13 13	...	<0.3	0.2	0.8
149...	M33 C710/	01 34 13.6	+30 33 42.5	5 49	...	<0.2	0.4	0.2

NOTES.—Units of right ascension are hours, minutes, and seconds, and units of declination are degrees, arcminutes, and arcseconds. R_{M33} is the M33 angular galactocentric radius in arcminutes and arcseconds. The fluxes are in units of 10^{-19} W cm $^{-2}$.

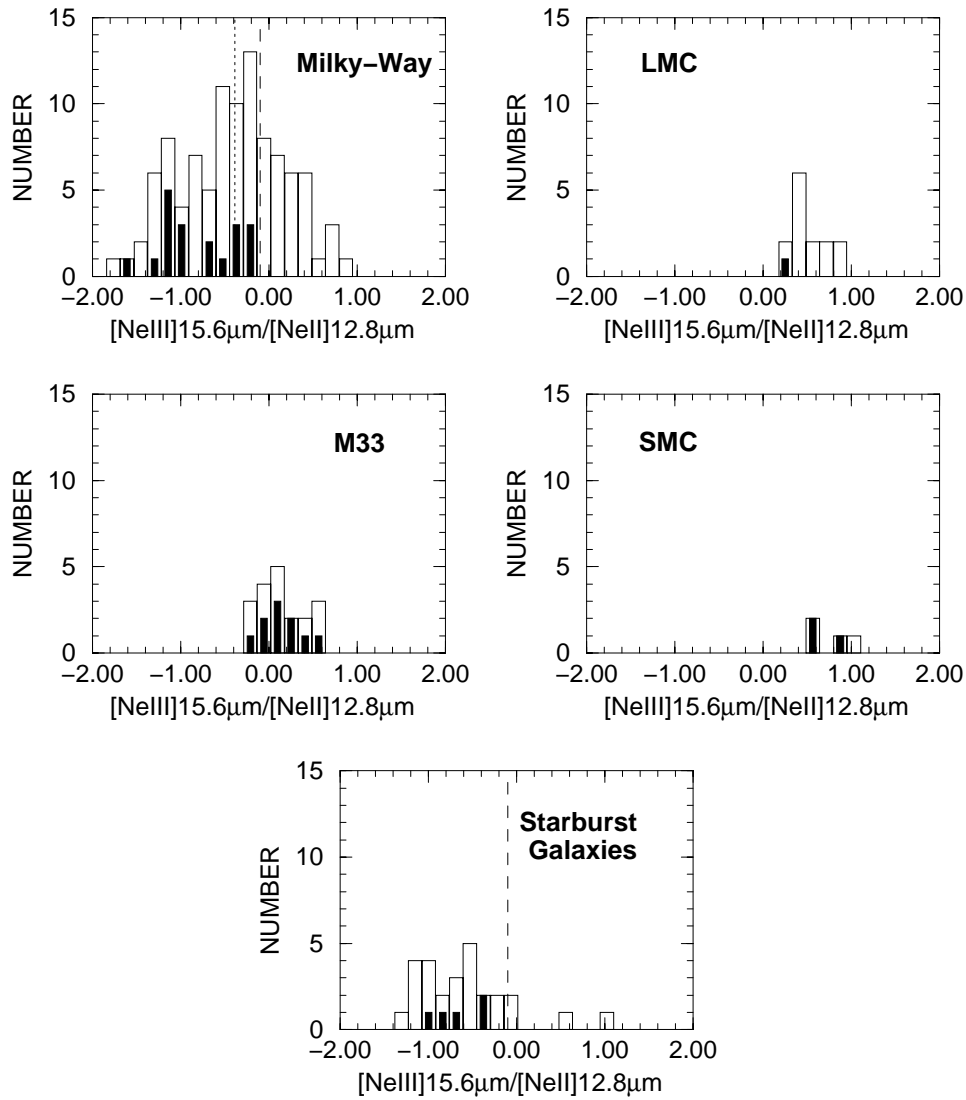


FIG. 1.—Histograms of the observed logarithmic $[\text{Ne III}] 15.6 \mu\text{m}/[\text{Ne II}] 12.8 \mu\text{m}$ ratio (not corrected for extinction) for sources in the our sample—the Galaxy, the LMC, the SMC, and M33, and also of extra-Galactic sources from Thornley et al. (2000). Filled bars designate sources whose ratios are uncertain. For the Milky Way and the starburst sample, these are all upper limits; for the LMC and SMC, lower limits; whereas in M33, both cases are mixed together. Our estimation of the integrated $[\text{Ne III}] 15.6 \mu\text{m}/[\text{Ne II}] 12.8 \mu\text{m}$ ratio for the Galaxy is overplotted as vertical long-dashed lines in both the Galactic and extra-Galactic histograms. The median $[\text{Ne III}] 15.6 \mu\text{m}/[\text{Ne II}] 12.8 \mu\text{m}$ ratio for the Galaxy is shown as the vertical short-dashed line in the histogram of the Galaxy. The Galaxy appears to have higher excitation ratio than most starburst galaxies.

important clue as to the origin of the excitation gradients, as we discuss in § 4.

The ionization potentials of Ar^+ , S^{++} , and Ne^+ are equal to 27.63 eV (~ 2 ryd), 34.79, and 40.96 eV (~ 3 ryd), respectively (see Fig. 6). Thus, the ratios $[\text{Ar III}] 8.99 \mu\text{m}/[\text{Ar II}] 6.99 \mu\text{m}$, $[\text{S IV}] 10.5 \mu\text{m}/[\text{S III}] 33.5 \mu\text{m}$, and $[\text{Ne III}] 15.6 \mu\text{m}/[\text{Ne II}] 12.8 \mu\text{m}$ constrain the shapes of the SEDs of the ionizing spectra over a range of several rydbergs. One possible representation for the data, which may give clues regarding the properties of the SEDs, is a diagnostic diagram combining two of these empirical ratios. In Figure 3 we plot the $[\text{Ar III}] 8.99 \mu\text{m}/[\text{Ar II}] 6.99 \mu\text{m}$ versus $[\text{Ne III}] 15.6 \mu\text{m}/[\text{Ne II}] 12.8 \mu\text{m}$ ratios for our sample. A good correlation is apparent, showing that nebular excitation is probed by both line ratios, and manifests the interrelation between the two spectral regions, $2 \text{ ryd} < \varepsilon < 3 \text{ ryd}$ and $\varepsilon > 3 \text{ ryd}$. A representative error bar for the data is shown in the lower right corner of the plot.

In order to connect this correlation in excitation space to position within the Galaxy, we display each source in the lower panel of Figure 3 as a symbol according to its galactocentric radius. Plus signs designate the inner kiloparsec in the Galaxy ($R_{\text{gal}} < 1 \text{ kpc}$), circles designate Galactic disk sources ($R_{\text{gal}} > 1 \text{ kpc}$), and asterisks designate extra-Galactic sources. From this diagram it is clear that the sources in the central kiloparsec of the Galaxy are all of low excitation. On the other hand, sources in the LMC are all of high excitation. Sources in the disk of the Galaxy show moderate levels of excitation.

3.2. Extinction and Gas Densities

We use the Brackett line ratio, $\text{Br}\alpha/\text{Br}\beta$ (for those sources for which both lines are measured) to deredden the fine-structure line intensities. We assume a foreground screen and adopt the Draine (1989) mid-IR extinction curve. For case B recombination, the intrinsic Brackett decrement

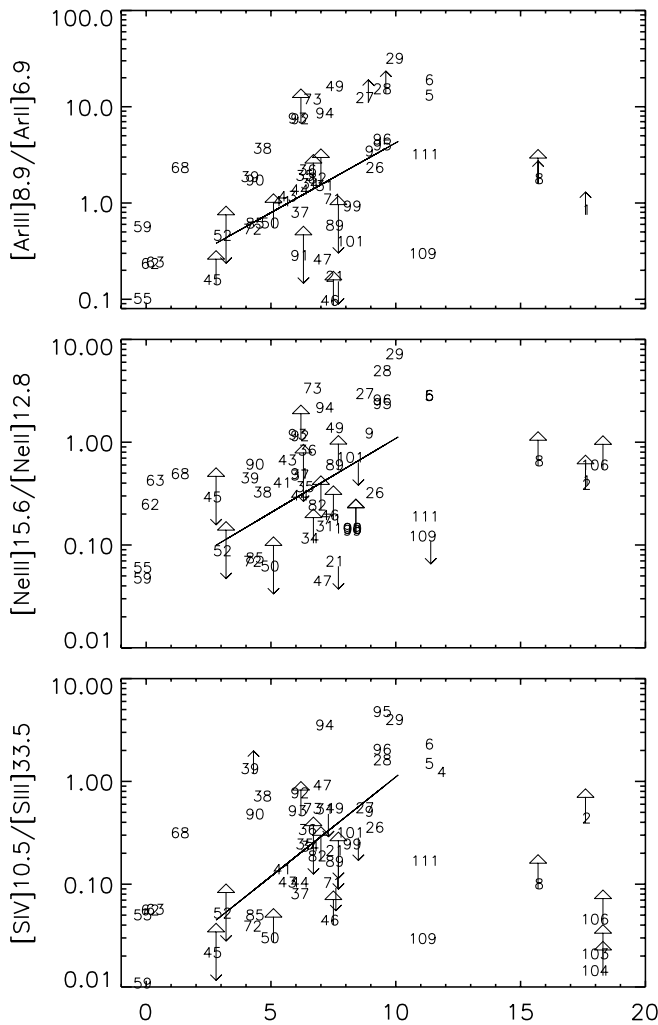


FIG. 2.—Excitation ratios vs. galactocentric radius for Galactic sources. The plot for $[\text{Ar III}] 8.9 \mu\text{m}/[\text{Ar II}] 6.99 \mu\text{m}$ is in the upper panel. In the middle panel we show the $[\text{Ne III}] 15.6 \mu\text{m}/[\text{Ne II}] 12.8 \mu\text{m}$ plot, and in the lower panel we show the $[\text{S IV}] 10.5 \mu\text{m}/[\text{S III}] 33.5 \mu\text{m}$ plot. A rise in the excitation toward the outer Galaxy is clear. Solid lines are fits to the gradients (for $2 \text{kpc} \leq R_{\text{gal}} \leq 11 \text{kpc}$), whose values are given in the text. We designate limits on the given quantities by small arrows. The larger arrows indicate lower limits resulting from uncertainties in the extinction correction.

ranges from 1.6 to 1.9 for gas temperatures between 5×10^3 and 2×10^4 K and densities between 10^2 and 10^4cm^{-3} . Figure 4 shows the Brackett ratio for the objects in our sample versus galactocentric radius.

It is evident that there are objects with unphysical Brackett ratios much below the optically thin ratio of ~ 1.7 . These objects generally correspond to sources with noisy low signal-to-noise spectra, and we discard them in our subsequent analysis. The extinction correction is most significant for the $[\text{Ar III}] 8.99 \mu\text{m}$ and $[\text{S IV}] 10.5 \mu\text{m}$ lines, which lie close to the mid-IR silicate absorption feature. For these lines, correction factors as large as 10–25 are implied by the Brackett decrements. The corrections for the other fine-structure lines are small. For some objects only an upper limit exists for $\text{Br}\beta$. We adopt the upper limit values to compute a minimum extinction correction for such objects. Objects with lower limit extinction corrections are indicated by the large arrows in the figures.

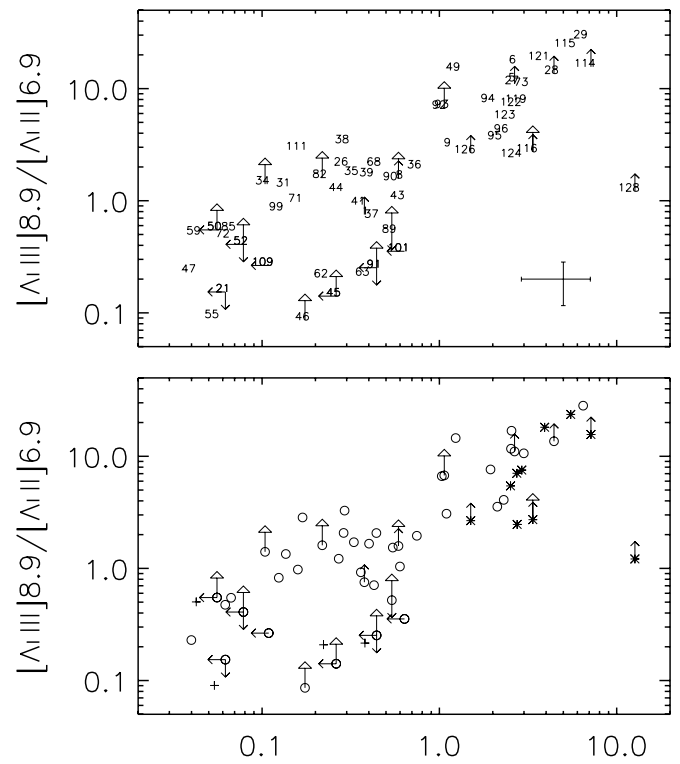


FIG. 3.—*Top panel*: $[\text{Ar III}] 8.99 \mu\text{m}/[\text{Ar II}] 6.99 \mu\text{m}$ vs. $[\text{Ne III}] 15.6 \mu\text{m}/[\text{Ne II}] 12.8 \mu\text{m}$ for the entire sample. The data points are represented by the source identifications in Tables 2, 5, and 6. A representative error bar for the data is shown in the lower right corner. *Bottom panel*: Same as above, with data points marked with symbols according to their galactocentric radius. Plus signs designate the inner kiloparsec (the Galaxy $R_{\text{gal}} < 1 \text{kpc}$), circles designate Galactic disk sources ($R_{\text{gal}} > 1 \text{kpc}$), and asterisks designate extra-Galactic sources.

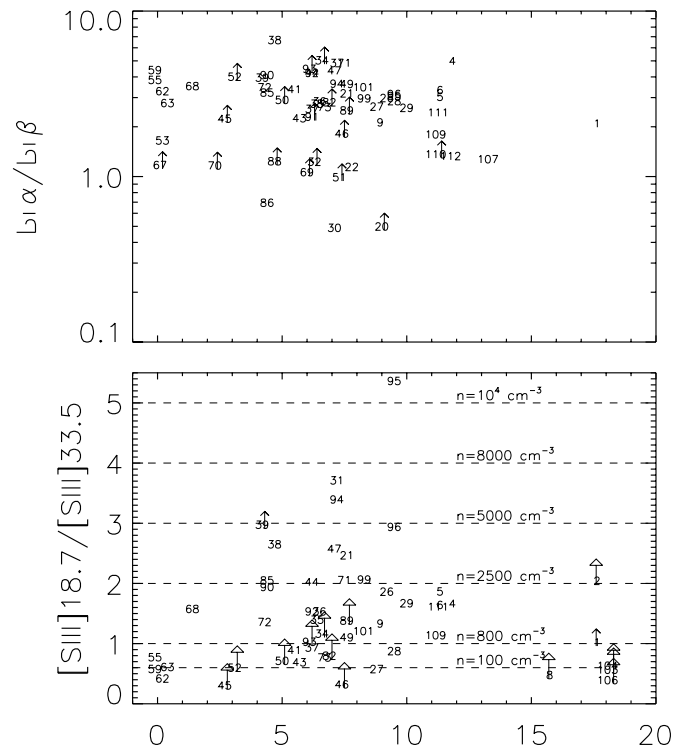


FIG. 4.— $\text{Br}\alpha/\text{Br}\beta$ ratio (*top panel*) and the $[\text{S III}] 18.7 \mu\text{m}/[\text{S III}] 33.5 \mu\text{m}$ ratio (*bottom panel*) for Galactic sources in our sample that have measured fluxes for these lines, as a function of the galactocentric radius.

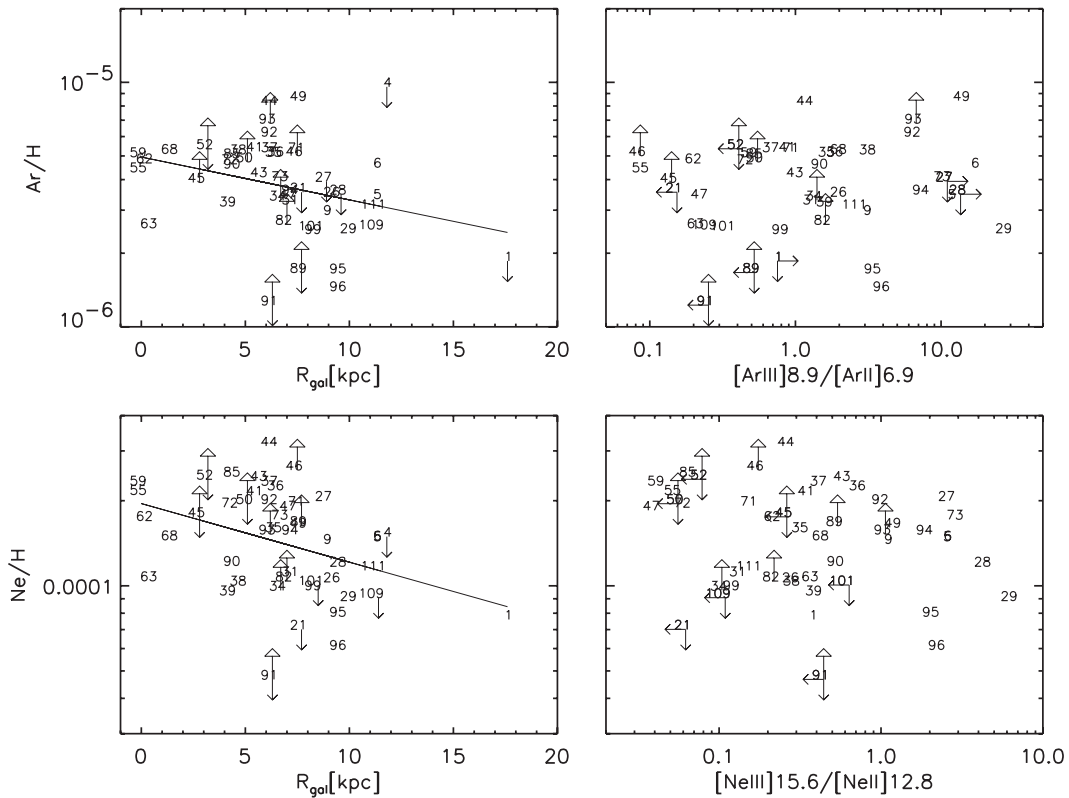


FIG. 5.—Argon and neon abundances vs. galactocentric radius (*left panels*) and vs. the corresponding excitation ratio (*right panels*). Solid lines are fits to the gradients (for $R_{\text{gal}} < 18$ kpc, whose values are given in the text).

The $[\text{S III}] 18.7 \mu\text{m}/[\text{S III}] 33.5 \mu\text{m}$ ratio was used as a gas density measure. The solid angle of the SWS aperture used to observe the $33.5 \mu\text{m}$ line is 1.75 times larger than the one used for the $18.7 \mu\text{m}$ line. Depending on source structure, this may require aperture corrections to the ratio up to about this factor. We have not attempted to derive these corrections for individual sources but note that observed ratios of ≈ 0.25 are possible for low-density extended sources.

In Figure 4 we display the $[\text{S III}] 18.7 \mu\text{m}/[\text{S III}] 33.5 \mu\text{m}$ versus galactocentric radius for the (extinction corrected) Galactic sources. The measured densities for our sample lie in the range of $\lesssim 100$ to $\sim 15,000 \text{ cm}^{-3}$ with a mean value of 800 cm^{-3} . Measurements of the S III ratio are also available for some of the LMC sources. These ratios lie in the range of 0.4–0.6, corresponding to densities $\lesssim 200 \text{ cm}^{-3}$.

3.3. Abundances

We have calculated the elemental abundances for neon and argon from the relative strengths of the fine-structure and Br α emission lines. In computing the fine-structure line emissivities, we adopt the IRON Project collision strengths (Saraph & Tully 1994 for $[\text{Ne II}]$; Butler & Zeippen 1994 for $[\text{Ne III}]$; Pelan & Berrington 1995 for $[\text{Ar II}]$; Galavis et al. 1995 for $[\text{Ar III}]$). (These data are also employed in the CLOUDY photoionization models that we discuss in § 4.) The critical densities ($\gtrsim 10^5 \text{ cm}^{-3}$) of the relevant neon and argon transitions are much larger than the estimated gas densities, so that collisional deexcitations are negligible. Because of the large ionization potential (4.7 ryd) of Ne^{++} , we assume that neon exists either as Ne^+ or Ne^{++} in the H II regions. The ionization potential of Ar^{++} is 3.0 ryd, very similar to that of Ne^+ . However, Ar^{+++} ions are

rapidly removed by charge transfer reactions with neutral hydrogen (Butler & Dalgarno 1980). In contrast, charge transfer neutralization is inefficient for Ne^{++} (Butler, Heil, & Dalgarno 1980). We therefore assume that negligible $[\text{Ar IV}]$ is produced in the nebulae even when $[\text{Ne III}]/[\text{Ne II}]$ is large. This is verified by our CLOUDY computations, which incorporate the Butler et al. charge transfer rate coefficients. Thus, we do not apply ionization “correction factors” in deriving the neon and argon abundances from our fine-structure line data.

For the singly ionized species, Ar^+ and Ne^+ , which have two fine-structure levels in their ground state, the emissivity is given by

$$j_{\text{II}} = n_e n_{q_{\text{II}}} h\nu_{\text{II}} \frac{X_{\text{II}}}{H}, \quad (6)$$

where n is the gas density, n_e is the electron density, q_{II} is the collisional excitation rate, and X_{II}/H is the abundance of the species relative to hydrogen. For the doubly ionized species, Ar^{++} and Ne^{++} , which have three fine-structure levels in their ground state, the emissivity is given by

$$j_{\text{III}} = n_e n (q_{12} + q_{13}) h\nu_{\text{III}} \frac{X_{\text{III}}}{H} = n_e n_{q_{\text{III}}} h\nu_{\text{III}} \frac{X_{\text{III}}}{H}, \quad (7)$$

where q_{12} and q_{13} are the collisional excitation rates between the first level and the second and third levels, respectively. The Br α emissivity

$$j_{\text{Br}\alpha} = \alpha_B(5 \rightarrow 4) n_e n_{\text{H}^+} h\nu_{\text{Br}\alpha}, \quad (8)$$

where n_{H^+} is ionized hydrogen density $\alpha_B(5 \rightarrow 4)$, is the case B effective recombination coefficient for Br α . We assume $n \approx n_{\text{H}^+}$.

It follows that the abundance, X/H , is given by

$$\frac{X}{H} = \frac{X_{\text{II}}}{H} + \frac{X_{\text{III}}}{H} = \frac{\alpha(5 \rightarrow 4)h\nu_{\text{Br}\alpha}}{j_{\text{Br}\alpha}} \left(\frac{j_{\text{II}}}{q_{\text{II}}h\nu_{\text{II}}} + \frac{j_{\text{III}}}{q_{\text{III}}h\nu_{\text{III}}} \right). \quad (9)$$

Inserting the basic atomic data, one gets

$$\begin{aligned} \frac{\text{Ne}}{H} &= 10^{-5} \times \frac{2.30f_{\text{Ne II}} + f_{\text{Ne III}}}{1.90f_{\text{Br}\alpha}}, \\ \frac{\text{Ar}}{H} &= 10^{-6} \times \frac{f_{\text{Ar II}} + 1.26f_{\text{Ar III}}}{1.43f_{\text{Br}\alpha}}, \end{aligned} \quad (10)$$

where f_x are the line fluxes.

Figure 5 shows the computed neon and argon abundances versus galactocentric radius for the Galactic sources. Both abundances show a decrease from the inner parts of the Galaxy outward. Both elements vary from ~ 2 times solar to ~ 1 times solar metallicities. The fitted gradients over the entire range of galactocentric radii are

$$\left[\frac{\text{Ne}}{H} \right] = -3.71(\pm 0.06) - 0.021(\pm 0.007)R_{\text{gal}}, \quad (11)$$

$$\left[\frac{\text{Ar}}{H} \right] = -5.31(\pm 0.06) - 0.018(\pm 0.008)R_{\text{gal}}, \quad (12)$$

where the solar metallicity values are $[\text{Ne}/H]_{\odot} = -3.92$ and $[\text{Ar}/H]_{\odot} = -5.60$ (Grevesse & Sauval 1998).

The statistical significance of our detected gradients is low. However, our results are consistent with previous studies. Afflerbach et al. (1997) found similar gradients, from twice solar metallicity in the inner Galaxy to lower values outward, in their study of O/H and S/H . Simpson et al. (1995) found a gradient in the neon abundance that is steeper than ours (-0.08 ± 0.02 dex kpc^{-1}), but their sample consists of only 18 sources. Simpson & Rubin (1990) also found the inner Galactic sources to be of about twice solar metallicity. In their preliminary study, Cox et al. (1999) show evidence of a neon abundance gradient as probed by the $[\text{Ne II}] 12.8 \mu\text{m}/\text{Br}\alpha$ ratio. However, their analysis did not include contributions due to Ne^{++} ions as probed by the $[\text{Ne III}]$ emission, which dominates in the high-excitation nebulae.

4. ANALYSIS

The aim of the following analysis is to obtain a theoretical fit to the empirical $[\text{Ar III}] 8.99 \mu\text{m}/[\text{Ar II}] 6.99 \mu\text{m}$ versus $[\text{Ne III}] 15.6 \mu\text{m}/[\text{Ne II}] 12.8 \mu\text{m}$ diagram shown in Figure 3. We consider a sequence of photoionization models in which we assume that the H II regions are ionized by single stars. We compute NLTE model atmospheres for high surface gravity dwarf and low gravity giant stars with a range of effective temperatures. In the nebular analysis we explore the effects of varying the gas density, ionization parameter, and metallicity. We also consider the effects of metallicity variations in the model atmosphere computations.

4.1. Models

We use the *WM-basic* stellar atmosphere code (Pauldrach et al. 2001)⁴ to compute the spectral energy dis-

tributions. These NLTE atmosphere computations include the hydrodynamical treatment of steady-state winds and mass loss and include the combined effects of line blocking and line blanketing. The *WM-basic* package employs up-to-date atomic data, which provide the basis for a detailed multilevel NLTE treatment of the metal ions, from C to Zn. As discussed by Pauldrach et al., a key (and unique) feature of our model atmospheres is that they successfully reproduce the spectral characteristics of hot stars as revealed by high-resolution far-UV spectroscopy. We use the NLTE atmospheres to construct model stars as input ionizing sources for the nebulae that we model using the photoionization code CLOUDY (Version C90.04; Ferland et al. 1998).⁵ We also carry out computations using the older generation LTE static atmospheres (Kurucz 1979, 1992).

In general, the NLTE wind models have “harder” SEDs compared to the hydrostatic LTE models (see also Schaerer & de Koter 1997). For a given stellar effective temperature, the NLTE atmospheres emit significantly larger fluxes of energetic photons. Figure 6 shows an example of the differences between the LTE and NLTE spectral energy distributions for an effective temperature $T_{\text{eff}} = 35,000$ K and surface gravity $\log g = 4.0$.

The relative deficiency in high energy photons ($\gtrsim 3$ ryd) in the LTE model is clear. The ionization edges of the relevant ions are overlaid on the spectra in this plot. The nebular ionization state, expressed by the ratios $[\text{Ne III}] 15.6 \mu\text{m}/[\text{Ne II}] 12.8 \mu\text{m}$ or $[\text{Ar III}] 8.99 \mu\text{m}/[\text{Ar II}] 6.99 \mu\text{m}$, is sensitive to the shape of the SED, and the NLTE models will generally produce greater excitation. It is apparent from Figure 6 that the difference in excitation produced by the LTE and NLTE atmospheres will be more pronounced in the $\text{Ne}^{++}/\text{Ne}^+$ ratio compared to $\text{Ar}^{++}/\text{Ar}^+$. This helps in breaking the degeneracy between the SED shape and the ionization parameter as factors that influence the ionization state of the gas.

We have computed model atmospheres for “representative” main sequence dwarfs ($\log g = 4.0$) as well as supergiants ($\log g = 3.25\text{--}3.75$) for T_{eff} ranging from 35,000 to 45,000 K, in steps of 10^3 K. We computed models for solar ($1 Z_{\odot}$; Grevesse & Sauval 1998), half-solar ($0.5 Z_{\odot}$), and twice-solar ($2 Z_{\odot}$) metallicities. The stellar wind opacities and resulting SEDs depend on the assumed

⁵ See also <http://www.pa.uky.edu/~gary/cloudy>.

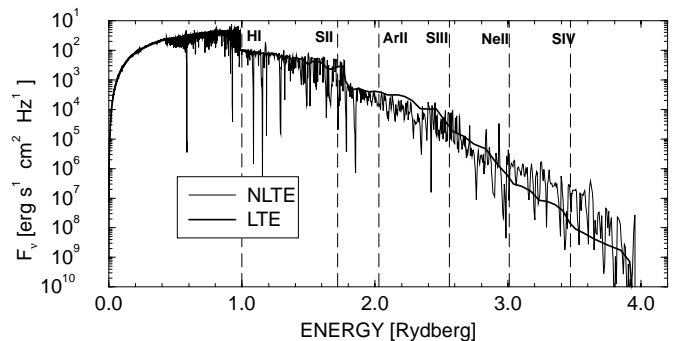


FIG. 6.—Comparison between the LTE and NLTE SEDs for $T_{\text{eff}} = 35,000$ K and $\log g = 4.0$. The ionization edges of the relevant ions are indicated by vertical dashed lines.

⁴ See also <http://www.usm.uni-muenchen.de/people/adi/adi.html>.

stellar mass-loss rates (Pauldrach et al. 2001). For each metallicity, we fix the mass-loss rates (and terminal wind velocities) using the empirically based wind momentum–luminosity relationship for O-star supergiants, giants, and dwarfs (Kudritzki & Puls 2000).

We represent the nebulae as optically thick Strömgren spheres and consider clouds with constant hydrogen densities ranging from 10^2 to $3 \times 10^3 \text{ cm}^{-3}$. We assume a gas filling factor $f = 1$. For each stellar effective temperature, T_{eff} , we compute the Lyman continuum photon emission rate

$$Q = 4\pi R_*^2 \int_{\nu_0}^{\infty} \frac{F_{\nu}(T_{\text{eff}})}{h\nu} d\nu (\text{s}^{-1}), \quad (13)$$

where $F_{\nu}(T_{\text{eff}})$ (in $\text{erg s}^{-1} \text{cm}^{-2} \text{Hz}^{-1}$) is the SED, ν_0 is the Lyman limit frequency, and R_* is the stellar radius ($\sim 10 R_{\odot}$ for O-type dwarfs and $\sim 20 R_{\odot}$ for giants).

The nebular ionization structure depends on the shape of the SED and also on the ionization parameter

$$U \equiv \frac{Q}{4\pi r_s^2 n c}, \quad (14)$$

where c is the speed of light, n is the nebular gas density, and r_s is the Strömgren radius given by

$$Q = \frac{4\pi}{3} \alpha_B r_s^3 n^2, \quad (15)$$

where α_B is the case B recombination coefficient. It follows that

$$U = \frac{1}{c} \left(\frac{n \alpha_B^2 Q}{36\pi} \right)^{1/3}. \quad (16)$$

Thus, for a fixed nebular density the ionization parameter is fully determined by the stellar atmosphere model. For a given density we determine U from the stellar model and compute the resulting $[\text{Ar III}] 8.99 \mu\text{m}/[\text{Ar II}] 6.99 \mu\text{m}$ and $[\text{Ne III}] 15.6 \mu\text{m}/[\text{Ne II}] 12.8 \mu\text{m}$ emission line ratios using CLOUDY. As a representative density, we set $n = 800 \text{ cm}^{-3}$ as determined from the S III density diagnostic (see § 3.3).

Tables 7, 8, and 9 summarize the parameters for the stellar atmospheres that we adopt as the ionizing sources in our photoionization computations. These parameters include the stellar effective temperature, surface gravity, stellar radius, wind parameters (mass-loss rate \dot{M} and the terminal velocity v_{∞}), and hydrogen photoionization rates for NLTE typical dwarfs and supergiants and for LTE dwarfs. The parameters are given for the half-solar, solar, and twice-solar metallicities.

4.2. Comparison with Observations

In Figure 7 we show the $[\text{Ar III}] 8.99 \mu\text{m}/[\text{Ar II}] 6.99 \mu\text{m}$ versus $[\text{Ne III}] 15.6 \mu\text{m}/[\text{Ne II}] 12.8 \mu\text{m}$ observations (Fig. 3) together with the model computations for the LTE (dwarf) and NLTE (dwarf and giant) stars for solar metallicity and a gas density of 800 cm^{-3} . The boldfaced numbers beside

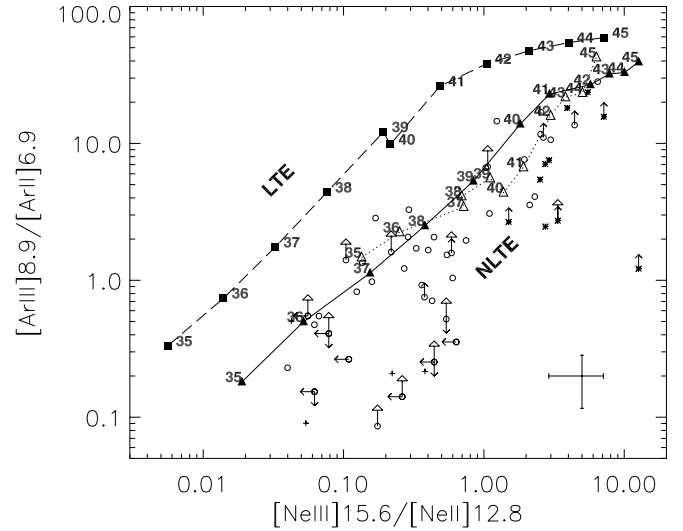


FIG. 7.— $[\text{Ar III}] 8.99 \mu\text{m}/[\text{Ar II}] 6.99 \mu\text{m}$ vs. $[\text{Ne III}] 15.6 \mu\text{m}/[\text{Ne II}] 12.8 \mu\text{m}$ diagnostic diagram. Boldfaced numbers indicate models. Triangles are $1 Z_{\odot}$ NLTE models. The dwarf sequence is designated by the solid line, and the supergiant sequence is designated by the dotted line. Squares are $1 Z_{\odot}$ LTE models. Models are designated by their effective temperature in units of 10^3 K . A representative error bar for the data is shown in the lower right corner.

TABLE 7

THE MODEL ATMOSPHERES PARAMETERS: STELLAR EFFECTIVE TEMPERATURE, SURFACE GRAVITY, STELLAR RADIUS, WIND PARAMETERS (\dot{M} AND v_{∞}) AND HYDROGEN PHOTOIONIZATION RATES OF OUR NLTE TYPICAL DWARFS

T_{eff} (K)	$\log g$ (cm s^{-2})	R_* (R_{\odot})	0.5 Z_{\odot}			1 Z_{\odot}			2 Z_{\odot}		
			$\log Q$ (s^{-1})	v_{∞} (km s^{-1})	$10^{-7}\dot{M}$ ($M_{\odot} \text{ yr}^{-1}$)	$\log Q$ (s^{-1})	v_{∞} (km s^{-1})	$10^{-7}\dot{M}$ ($M_{\odot} \text{ yr}^{-1}$)	$\log Q$ (s^{-1})	v_{∞} (km s^{-1})	$10^{-7}\dot{M}$ ($M_{\odot} \text{ yr}^{-1}$)
35000.....	4.0	9.0	48.37	2000	0.8	48.35	2004	1.6	48.37	2008	3.4
36000.....	4.0	9.2	48.52	2079	1.0	48.51	2093	1.9	48.53	2086	3.9
37000.....	4.0	9.4	48.67	2158	1.2	48.68	2177	2.3	48.68	2181	4.6
38000.....	4.0	9.6	48.76	2283	1.5	48.73	2272	2.8	48.73	2277	5.2
39000.....	4.0	9.8	48.88	2358	1.8	48.87	2362	3.3	48.85	2365	6.1
40000.....	4.0	10.0	48.99	2450	2.2	48.98	2450	4.0	48.98	2460	7.0
41000.....	4.0	10.2	49.09	2548	2.8	49.08	2541	4.8	49.07	2564	8.3
42000.....	4.0	10.4	49.19	2637	3.4	49.18	2640	5.7	49.16	2620	9.6
43000.....	4.0	10.6	49.26	2732	4.0	49.26	2719	6.7	49.26	2722	11.0
44000.....	4.0	10.8	49.34	2803	4.9	49.33	2806	7.8	49.32	2800	13.0
45000.....	4.0	11.0	49.42	2894	5.8	49.40	2923	9.1	49.39	2900	14.0

NOTE.—The parameters are given for half-solar, solar, and twice-solar metallicities.

TABLE 8

THE MODEL ATMOSPHERES PARAMETERS OF OUR NLTE TYPICAL GIANTS FOR HALF-SOLAR, SOLAR, AND TWICE-SOLAR METALLICITIES

T_{eff} (K)	$\log g$ (cm s^{-2})	R_* (R_\odot)	0.5 Z_\odot			1 Z_\odot			2 Z_\odot		
			$\log Q$ (s^{-1})	v_∞ (km s^{-1})	$10^{-7}\dot{M}$ ($M_\odot \text{ yr}^{-1}$)	$\log Q$ (s^{-1})	v_∞ (km s^{-1})	$10^{-7}\dot{M}$ ($M_\odot \text{ yr}^{-1}$)	$\log Q$ (s^{-1})	v_∞ (km s^{-1})	$10^{-7}\dot{M}$ ($M_\odot \text{ yr}^{-1}$)
35000.....	3.25	24.0	49.54	1988	48	49.54	1998	63	49.52	2008	83
36000.....	3.30	23.4	49.60	2058	52	49.60	2061	69	49.59	2083	91
37000.....	3.35	22.8	49.64	2122	54	49.63	2125	74	49.62	2128	99
38000.....	3.40	22.2	49.65	2172	58	49.67	2180	78	49.66	2193	110
39000.....	3.45	21.6	49.72	2227	61	49.69	2235	83	49.70	2240	110
40000.....	3.50	21.0	49.74	2313	64	49.75	2311	88	49.74	2329	120
41000.....	3.55	20.4	49.79	2364	66	49.76	2367	91	49.77	2376	130
42000.....	3.60	19.8	49.81	2424	68	49.78	2426	95	49.79	2431	140
43000.....	3.65	19.2	49.84	2493	70	49.85	2483	100	49.82	2490	140
44000.....	3.70	18.6	49.86	2556	71	49.86	2548	100	49.85	2569	150
45000.....	3.75	18.0	49.87	2609	73	49.88	2610	110	49.87	2618	160

each model point give the T_{eff} of the corresponding star in units of 10^3 K. A representative error bar for the data is shown in the lower right corner of the plot.

For all sequences the predicted nebular excitation increases with increasing effective temperature of the photoionizing star. However, the LTE and NLTE models are clearly offset from one another, and it is evident that the NLTE sequences provide a much better fit to the observed excitation correlation. For a given $[\text{Ar III}] 8.99 \mu\text{m}/[\text{Ar II}] 6.99 \mu\text{m}$ ratio, the LTE models predict $[\text{Ne III}] 15.6 \mu\text{m}/[\text{Ne II}] 12.8 \mu\text{m}$ ratios that are factors of ~ 10 smaller than observed. This discrepancy appears to be almost entirely eliminated in the NLTE sequences. The NLTE fit may actually be even better than is indicated by Figure 7 since some of the scatter is likely due to underestimated extinction corrections for the $[\text{Ar III}] 8.99 \mu\text{m}$ line.

The key difference between the LTE and NLTE models lies in the different spectral shapes of their photoionizing continua. This is illustrated in Figure 8, where for each effective temperature in the LTE and NLTE sequences we plot the fractions Q_{argon}/Q versus Q_{neon}/Q , where Q_{argon} is the photon emission rate for photons above the $\text{Ar}^+ 27.6 \text{ eV}$ ionization threshold, Q_{neon} is the emission rate above the $\text{Ne}^+ 40.96 \text{ eV}$ threshold, and Q is the total Lyman continuum emission rate. The SEDs harden as T_{eff} increases, and both ratios Q_{argon}/Q and Q_{neon}/Q increase. For a given value of Q_{argon}/Q , the LTE atmosphere models produce much

smaller values of Q_{neon}/Q than the NLTE atmospheres. This is the behavior that is essentially represented in the $[\text{Ar III}] 8.99 \mu\text{m}/[\text{Ar II}] 6.99 \mu\text{m}$ versus $[\text{Ne III}] 15.6 \mu\text{m}/[\text{Ne II}] 12.8 \mu\text{m}$ excitation diagram. The *ISO* fine-structure data thus provide direct empirical evidence for the improved accuracy of the NLTE atmosphere SEDs in the Lyman continuum range. The NLTE sequence also indicates that for most of the displayed H II regions the effective temperatures of the exciting stars plausibly lie in the range of 35,000–45,000 K.

We have examined the dependence of the model results on the ionization parameter by considering variations in both Q and n (see eq. [16]). Although Q is fixed by the stellar model, we have verified that changing Q (for a fixed SED) simply moves the computed points along the (approximate) diagonal lines defined by each sequence of models. Larger values of Q could be produced by clusters of (identical) stars of given effective temperature. For an H II region excited by a mix of stars, one would expect the high SED energies to be dominated by hotter stars and the low energies by cooler stars. We will explore the effects of realistic clusters containing a synthesized distribution of stars

TABLE 9

THE MODEL ATMOSPHERES PARAMETERS OF THE LTE DWARFS FOR SOLAR METALLICITY

T_{eff} (K)	$\log g$ (cm s^{-2})	R_* (R_\odot)	$\log Q$ (s^{-1})
35000.....	4.0	9.0	48.43
36000.....	4.0	9.2	48.57
37000.....	4.0	9.4	48.70
38000.....	4.0	9.6	48.81
39000.....	4.0	9.8	48.92
40000.....	4.5	10.0	48.96
41000.....	4.5	10.2	49.05
42000.....	4.5	10.4	49.14
43000.....	4.5	10.6	49.23
44000.....	4.5	10.8	49.31
45000.....	4.5	11.0	49.38

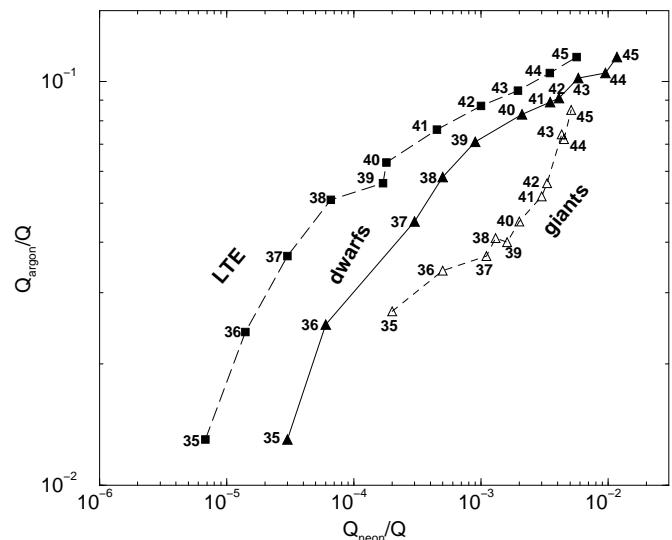


FIG. 8.—Fraction of photons that can ionize Ar^+ , Q_{argon}/Q , vs. the fraction for Ne^+ , Q_{neon}/Q , for each one of the model SEDs. The plot follows exactly the behavior of the models in the excitation ratios diagram, Fig. 7.

and associated cluster SEDs in a later paper. Variations in the assumed density (in the range of 10^2 to $3 \times 10^3 \text{ cm}^{-3}$) induce only small shifts in the positions of the computed model sequences.

In Figure 9 we show the NLTE dwarfs and LTE model sequences for nebular densities of 100, 800, and $3 \times 10^3 \text{ cm}^{-3}$. We conclude that the LTE sequence cannot be reconciled with the data by varying either Q or n .

In order to investigate the influence of varying the metallicity, we show in Figure 10 results for three sequences of NLTE atmosphere models of dwarfs—computed assuming half-solar, solar, and twice-solar metallicities. We varied the metallicity self-consistently in the nebulae and in the stellar atmospheres. Both of these variations affect the computed line ratios. Lower nebular metallicity results in higher gas temperatures, reduced recombination rates, and therefore slightly higher excitation. Aflerbach et al. (1997) found a similar trend in their study, but they also stressed the need for exploring the effects of metallicity variations in the stellar atmospheres as well. We have done this here and find that such variations have a somewhat larger effect on the computed line ratios. For a given effective temperature the SED hardens with decreasing metallicity, because of decreased line blocking in the stellar atmosphere winds. This effect is primarily significant above $\sim 2.5 \text{ ryd}$. At these energies the blocking is dominated by many Fe IV, Fe V, and Fe VI lines, which are mainly optically thick near the wind sonic point and optically thin in the outer wind region. As

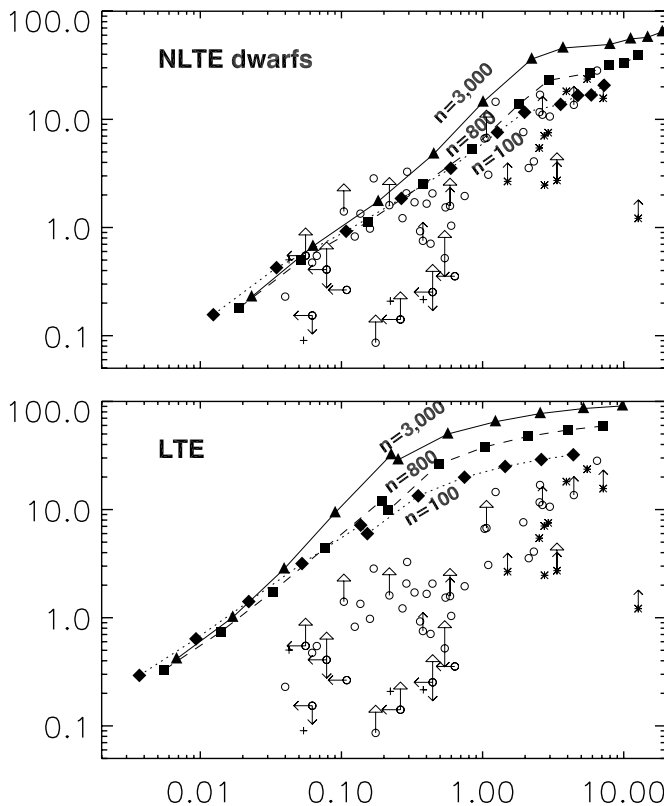


FIG. 9.—[Ar III] 8.99 μm /[Ar II] 6.99 μm vs. [Ne III] 15.6 μm /[Ne II] 12.8 μm diagnostic diagram with the NLTE dwarf models (top panel) and the LTE models (bottom panel) of various gas densities overplotted. Triangles are $3,000 \text{ cm}^{-3}$ models, squares are 800 cm^{-3} models, and diamonds are 100 cm^{-3} models. All model sequences are composed of models with effective temperatures in the range 35 (bottom left) to 45 (top right) $\times 10^3 \text{ K}$.

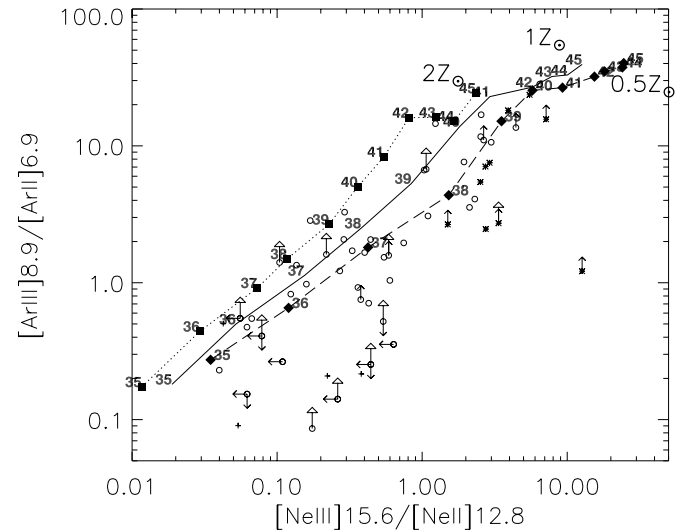


FIG. 10.—[Ar III] 8.99 μm /[Ar II] 6.99 μm vs. [Ne III] 15.6 μm /[Ne II] 12.8 μm diagnostic diagram for dwarf models with various metallicities. Triangles are solar metallicity models. Diamonds and squares indicate $0.5 Z_{\odot}$ and $2 Z_{\odot}$, respectively. Models are designated by their effective temperature in units of 10^3 K .

the metallicity is increased, the Fe lines remain optically thick to higher velocities, thus enhancing the blocking influence in this frequency regime. However, below $\sim 2.5 \text{ ryd}$ the blocking is dominated by C, N, O, Ne, and Ar. The corresponding lines are mainly optically thick in the entire wind region. Changes in metallicity therefore do not significantly affect the emergent (blocked) fluxes below 2.5 ryd. Therefore, varying the metallicity has a larger effect on the [Ne III] 15.6 μm /[Ne II] 12.8 μm ratio than on the [Ar III] 8.99 μm /[Ar II] 6.99 μm ratio, as indicated in Figure 10. For example, for a 40,000 K star, increasing the nebular and stellar metallicity from 0.5 to $2 Z_{\odot}$ reduces the [Ar III] 8.99 μm /[Ar II] 6.99 μm ratio by a factor of ~ 5 and the [Ne III] 15.6 μm /[Ne II] 12.8 μm ratio by a factor of ~ 20 .

Figure 10 also demonstrates that the excitation in the LMC nebulae (indicated by asterisks) is plausibly enhanced, at least in part, by the reduced metallicity of the LMC. However, the low excitation of the inner Galaxy sources (indicated by the crosses) is probably *not* due to their large metallicities, since these objects appear to have relatively large [Ne III] 15.6 μm /[Ne II] 12.8 μm ratios for their [Ar III] 8.99 μm /[Ar II] 6.99 μm ratios, whereas increasing the metallicity should selectively *reduce* the [Ne III] 15.6 μm /[Ne II] 12.8 μm ratio. The low excitation of the inner Galaxy sources is most likely due to lower effective temperatures of the stellar (or cluster) sources. In this respect these objects may resemble the typical low-excitation sources observed in the starburst sample of Thornley et al. (2000).

5. DISCUSSION AND SUMMARY

We have not attempted detailed modeling of individual sources in this paper. However, as we have shown, the ensemble of Galactic fine-structure emission line data provides empirical support for the generally harder photoionizing SEDs predicted in NLTE wind-driven line-blocked models of hot-star atmospheres. In particular, such models can readily account for the presence of high-excitation

[Ne III] emission lines in nebular spectra. Earlier studies that had relied on LTE atmospheres in the nebular analysis were unable to account for the observed [Ne III] emission and underpredicted the line intensities by factors of ~ 10 (e.g., Baldwin et al. 1991; Rubin et al. 1991; Simpson et al. 1995). Our study largely resolves this issue and supports the suggestions of Sellmaier et al. (1996) and Stasinska & Schaerer (1997) that this “Ne III problem” was due primarily to a significant underprediction of Lyman continuum photons above ~ 40 eV in the Kurucz LTE atmospheres.

This conclusion has important consequences for the interpretation of extra-Galactic fine-structure line observations. Thornley et al. (2000) carried out detailed starburst modeling of the [Ne III] $15.6 \mu\text{m}$ /[Ne II] $12.8 \mu\text{m}$ ratio expected from H II regions ionized by clusters of stars in which the stellar SEDs were modeled using the new-generation NLTE atmospheres. Given that the hottest stars in such models easily produce large nebular [Ne III] $15.6 \mu\text{m}$ /[Ne II] $12.8 \mu\text{m}$ ratios, the low ratios actually observed led to the conclusion that the relative number of hot stars is small because of aging of the starburst systems. Our analysis supports the conclusion that low [Ne III] $15.6 \mu\text{m}$ /[Ne II] $12.8 \mu\text{m}$ ratios require the removal of the hottest stars as dominant contributors to the ionization of the starburst galaxies.

We summarize our key results. We have compiled archival mid-IR *ISO-SWS* fine-structure line and H II recombination line observations from H II regions in the Galaxy, the LMC, SMC, and M33. We find that

1. There is a steep outward increase in excitation in the Galaxy as probed by the fine-structure line ratios [Ne III] $15.6 \mu\text{m}$ /[Ne II] $12.8 \mu\text{m}$, [Ar III] $8.99 \mu\text{m}$ /[Ar II] $6.99 \mu\text{m}$, and [S III] $18.7 \mu\text{m}$ /[S II] $33.5 \mu\text{m}$. Sources in the central

kiloparsec of the Galaxy show the lowest levels of excitation, and the LMC and SMC sources show the highest excitation level.

2. There is a slight decrease in metallicity from $\sim 2 Z_{\odot}$ in the Galactic center to $\sim 1 Z_{\odot}$ in the outer disk.

3. The increase in nebular excitation across the Galactic disk is likely due mainly to a rise in the typical effective temperatures of the exciting stars rather than a hardening of the stellar SEDs and enhanced nebular excitation associated with the decline in metallicity at fixed effective temperature.

4. By comparing models to observations, we find that the NLTE wind model atmospheres represent an impressive improvement in the realistic description of hot-star ionizing spectra (compared to LTE static models). In particular, the [Ne III] emission observed in Galactic H II regions is readily accounted for by these atmospheres.

5. We estimate an “integrated” [Ne III] $15.6 \mu\text{m}$ /[Ne II] $12.8 \mu\text{m}$ ratio of 0.8 for the Galaxy, well inside the range of values found for starburst galaxies. The good fit of the NLTE models to the data supports the suggestion by Thornley et al. (2000) that the observed [Ne III] $15.6 \mu\text{m}$ /[Ne II] $12.8 \mu\text{m}$ ratio in starburst galaxies is small because of aging effects.

We thank Roland Tacke and Julia Morfill for help with the data reduction and Tadziu Hoffmann for his assistance with the *WM-basic* program. We thank Gary Ferland and Hagai Netzer for discussions and the anonymous referee for helpful suggestions. The *ISO* spectrometer data center at MPE is supported by DLR under grants 50 QI 8610 8 and 50 QI 9402 3. Our research is supported by the German-Israeli Foundation (grant I-0551-186.07/97).

REFERENCES

- Afflerbach, A., Churchwell, E., Acord, J. M., Hofner, P., Kurtz, S., & Depree, C. G. 1996, *ApJS*, 106, 423
- Afflerbach, A., Churchwell, E., & Werner, M. W. 1997, *ApJ*, 478, 190
- Alexander, T., Lutz, D., Sturm, E., Genzel, R., Sternberg, A., & Netzer, H. 2000, *ApJ*, 536, 710
- Alexander, T., Sturm, E., Lutz, D., Sternberg, A., Netzer, H., & Genzel, R. 1999, *ApJ*, 512, 204
- Baldwin, J. A., Ferland, G. J., Martin, P. G., Corbin, M. R., Cota, M. A., Peterson, B. M., & Slettebak, A. 1991, *ApJ*, 374, 580
- Blitz, L., Fich, M., & Stark, A. A. 1982, *ApJS*, 49, 183
- Brand, J., et al. 1984, *A&A*, 139, 181
- Braz, M. A., & Epchtein, N. 1983, *A&AS*, 54, 167
- Bronfman, L., Nyman, L.-A., & May, J. 1996, *A&AS*, 115, 81
- Butler, K., & Dalgarno, A. 1980, *ApJ*, 241, 838
- Butler, K., Heil, T. G., & Dalgarno, A. 1980, *ApJ*, 241, 442
- Butler, K., & Zeppen, C. J. 1994, *A&AS*, 108, 1
- Caswell, J. L., Batchelor, R. A., Förster, J. R., & Wellington, K. J. 1989, *Australian J. Phys.*, 42, 331
- Caswell, J. L., & Haynes, R. F. 1987, *A&A*, 171, 261
- Churchwell, E., Walmsley, C. M., & Cesaroni, R. 1990, *A&AS*, 83, 119
- Cox, P., et al. 1999, in *The Universe as Seen by ISO*, ed. P. Cox & M. F. Kessler (ESA SP-427; Noordwijk: ESA), 631
- de Graauw, T., et al. 1996, *A&A*, 315, L49
- Draine, B. T. 1989, in *Infrared Spectroscopy in Astronomy*, ed. A. C. H. Glasse, M. F. Kessler, R. Gonzalez Riestra, & B. Kaldeich-Schürmann (ESA SP-290; Noordwijk: ESA), 93
- Ferland, G. J., Korista, K. T., Verner, D. A., Ferguson, J. W., Kingdon, J. B., & Verner, E. M. 1998, *PASP*, 110, 761
- Förster Schreiber, N. M., et al. 2001b, *ApJ*, submitted
- Förster Schreiber, N. M., Genzel, R., Lutz, D., Kunze, D., & Sternberg, A. 2001a, *ApJ*, 552, 544
- Galavis, M. E., et al. 1995, *A&AS*, 111, 347
- Genzel, R., & Cesarsky, J. S. 2000, *ARA&A*, 38, 761
- Genzel, R., et al. 1998, *ApJ*, 498, 579
- Grevesse, N., & Sauval, A. J. 1998, *Space Sci. Rev.*, 85, 161
- Henry, R. B. C., & Howard, J. W. 1995, *ApJ*, 438, 170
- Honma, M., & Sofue, Y. 1997, *PASJ*, 49, 453
- Huang, M., et al. 1999, *ApJ*, 517, 282
- Kessler, M. F., et al. 1996, *A&A*, 315, L27
- Kudritzki, R. P., & Puls, J. 2000, *ARA&A*, 38, 613
- Kunze, D., et al. 1996, *A&A*, 315, L101
- Kurucz, R. L. 1979, *ApJS*, 40, 1
- . 1992, *Rev. Mexicana Astron. Astrofis.*, 23, 181
- Lang, C. C., Figer, D. F., Goss, W. M., & Morris, M. 1999, *AJ*, 118, 2327
- Lockman, F. J. 1989, *ApJS*, 71, 469
- Lutz, D., et al. 1996, *A&A*, 315, L137
- Martin-Hernández, N. L., et al. 2000, in *ISO Beyond the Peaks: Proceedings of the Second ISO Workshop on Analytical Spectroscopy*, ed. A. Salama, M. F. Kessler, K. Leech, & B. Schulz (ESA-SP 456; Noordwijk: ESA), 135
- Pauldrach, A. W. A., Hoffmann, T. L., & Lennon, M. 2001, *A&A*, 375, 161
- Pelan, J., & Berrington, K. A. 1995, *A&AS*, 110, 209
- Rigopoulou, D., et al. 1996, *A&A*, 315, L125
- Rigopoulou, D., Spoon, H. W. W., Genzel, R., Lutz, D., Moorwood, A. F. M., & Tran, Q. D. 1999, *AJ*, 118, 2625
- Rodríguez-Fernández, N. J., Martín-Pintado, J., & de Vicente, P. 2001, *A&A*, 377, 631
- Roelfsema, P. R., Cox, P., Baluteau, J.-P., & Peeters, E. 1999, in *The Physics and Chemistry of the Interstellar Medium*, ed. V. Ossenkopf, J. Stutzki, & G. Winnewisser (Herdecke: GCA), 116
- Rohlfs, K., & Kreitschmann, J. 1987, *A&A*, 178, 95
- Rosenthal, D., Bertoldi, F., & Drapatz, S. 2000, *A&A*, 356, 705
- Rubin, R. H., Simpson, J. P., Haas, M. R., & Erickson, E. F. 1991, *PASP*, 103, 834
- Saraph, H. E., & Tully, J. A. 1994, *A&AS*, 107, 29
- Schaerer, D., & de Koter, A. 1997, *A&A*, 322, 598
- Sellmaier, F. H., Yamamoto, T., Pauldrach, A. W. A., & Rubin, R. H. 1996, *A&A*, 305, L37
- Shepherd, D. S., & Churchwell, E. 1996, *ApJ*, 457, 267
- Shields, G. A. 1990, *ARA&A*, 28, 525
- Shields, G. A., & Tinsley, B. M. 1976, *ApJ*, 203, 66
- Simpson, J. P., Colgan, S. W. J., Rubin, R. H., Erickson, E. F., & Haas, M. R. 1995, *ApJ*, 444, 721
- Simpson, J. P., & Rubin, R. H. 1990, *ApJ*, 354, 165

- Slysh, V. I., Kalenskii, S. V., Val'tts, I. E., & Otrupcek, R. 1994, MNRAS, 268, 464
- Stasinska, G., & Schaerer, D. 1997, A&A, 322, 615
- Sturm, E., et al. 1997, AAS, 190, 4004
- Szymczak, M., Hrynek, G., & Kus, A. J. 2000, A&AS, 143, 269
- Thornley, M. D., Förster Schreiber, N. M., Lutz, D., Genzel, R., Spoon, H. W. W., Kunze, D., & Sternberg, A. 2000, ApJ, 539, 641
- van den Ancker, M. E., Tielens, A. G. M., & Wesselius, P. R. 2000, A&A, 358, 1035
- van Dishoeck, E. F., Wright, C. M., Cernicharo, J., González-Alfonso, E., de Graauw, T., Helmich, F. P., & Vandenbussche, B. 1998, ApJ, 502, L173
- Walsh, A. J., Hyland, A. R., Robinson, G., & Burton, M. G. 1997, MNRAS, 291, 261
- Wink, J. E., Altenhoff, W. J., & Mezger, P. G. 1982, A&A, 108, 227
- Wink, J. E., Wilson, T. L., & Bieging, J. H. 1983, A&A, 127, 211
- Wouterloot, J. G. A., & Brand, C. 1989, A&AS, 80, 149

ERRATUM: “THE EXCITATION AND METALLICITY OF GALACTIC H II REGIONS FROM *ISO-SWS* OBSERVATIONS OF MID-INFRARED FINE-STRUCTURE LINES” (ApJ, 566, 880 [2002])

URIEL GIVEON AND AMIEL STERNBERG

School of Physics and Astronomy and the Wise Observatory, Tel Aviv University; giveon@wise.tau.ac.il, amiel@wise.tau.ac.il

DIETER LUTZ AND HELMUT FEUCHTGRUBER

Max-Planck-Institut für Extraterrestrische Physik; lutz@mpe.mpg.de, fgb@mpe.mpg.de

AND

A. W. A. PAULDRACH

Institute for Astronomy and Astrophysics of Munich University; uh10107@usm.uni-muenchen.de

Because of an error at the Press, several figures were published with incorrect or missing axis labels. Figures 2, 3, 4, and 9 are correctly reproduced below. The Press sincerely regrets the error.

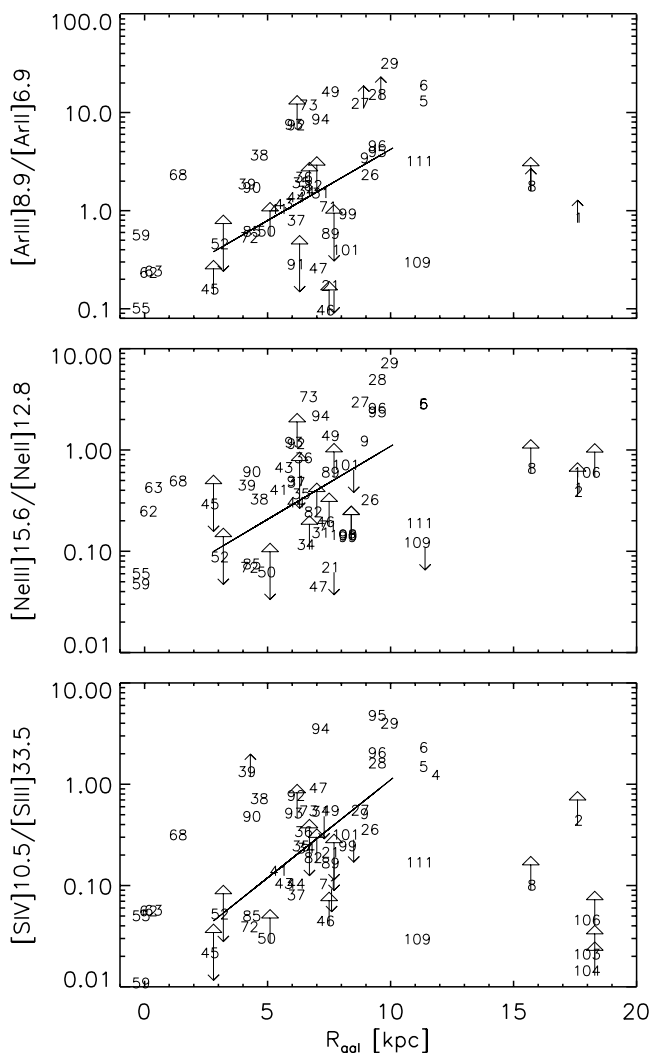


FIG. 2.—Excitation ratios vs. galactocentric radius for Galactic sources. The plot for [Ar III] 8.99 μm /[Ar II] 6.99 μm is in the upper panel. In the middle panel we show the [Ne III] 15.6 μm /[Ne II] 12.8 μm plot, and [S IV] 10.5 μm /[S III] 33.5 μm is in the lower panel. A rise in the excitation toward the outer Galaxy is clear. Solid lines are fits to the gradients (for $2 \text{ kpc} \leq R_{\text{gal}} \leq 11 \text{ kpc}$), whose values are given in the text. We designate limits on the given quantities by small arrows. The larger arrows indicate lower limits resulting from uncertainties in the extinction correction.

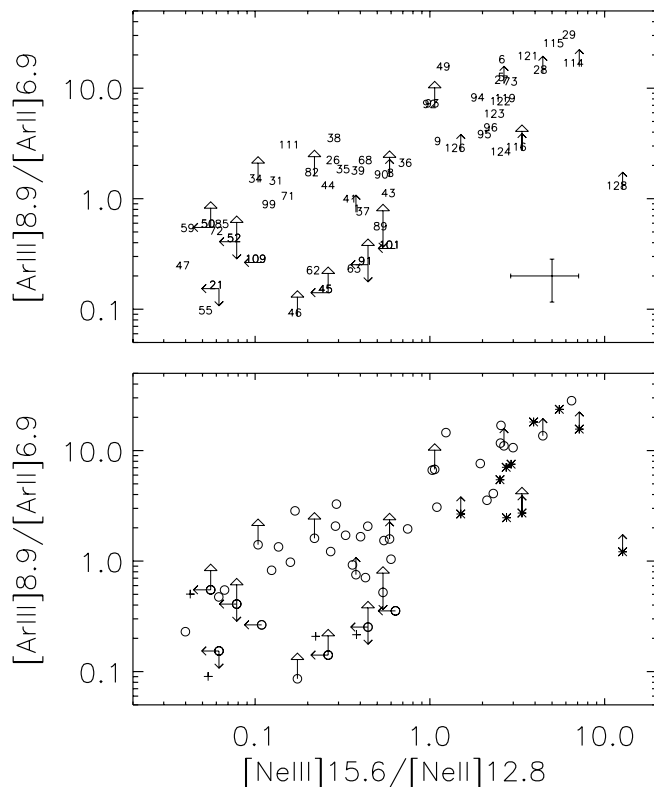


FIG. 3.—*Top panel:* [Ar III] 8.99 μm /[Ar II] 6.99 μm vs. [Ne III] 15.6 μm /[Ne II] 12.8 μm for the entire sample. The data points are represented by the source identifications in Tables 2, 5, and 6. A representative error bar for the data is shown in the lower right corner. *Bottom panel:* Same as above, with data points marked with symbols according to their galactocentric radius. Pluses designate the inner kiloparsec in the Galaxy ($R_{\text{gal}} < 1 \text{ kpc}$), circles designate Galactic disk sources ($R_{\text{gal}} > 1 \text{ kpc}$), and asterisks designate extra-Galactic sources.

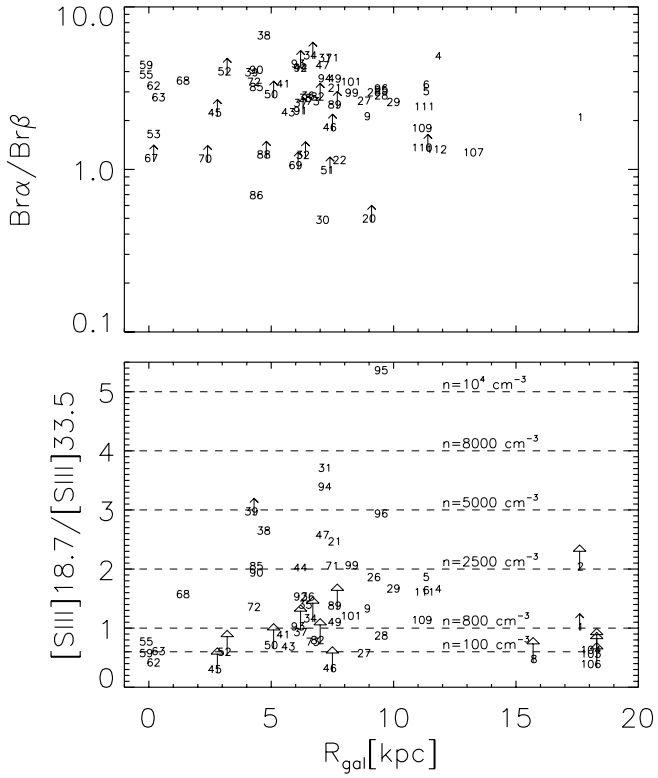


FIG. 4.— $\text{Br}\alpha/\text{Br}\beta$ ratio (*top panel*) and the $[\text{S III}] 18.7 / [\text{S III}] 33.5$ ratio (*bottom panel*) for Galactic sources in our sample that have measured fluxes for these lines, as a function of the galactocentric radius.

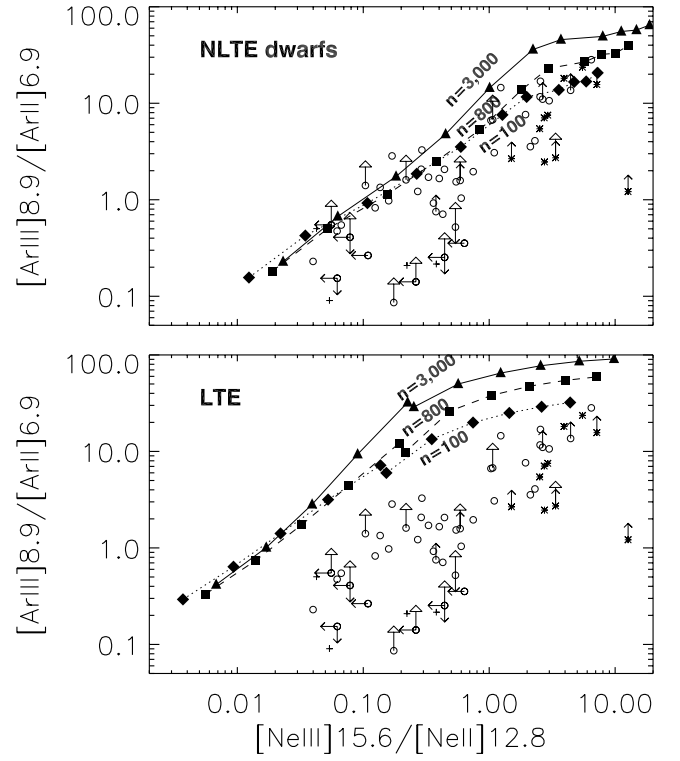


FIG. 9.— $[\text{Ar III}] 8.99 \mu\text{m} / [\text{Ar II}] 6.99 \mu\text{m}$ vs. $[\text{Ne III}] 15.6 \mu\text{m} / [\text{Ne II}] 12.8 \mu\text{m}$ diagnostic diagram with the NLTE dwarf models (*top panel*) and the LTE models (*bottom panel*) of various gas densities overplotted. Triangles are 3000 cm^{-3} models, squares are 800 cm^{-3} models, and diamonds are 100 cm^{-3} models. All model sequences are composed of models with effective temperatures in the range 35 (*bottom left*) to 45 (*top right*) $\times 10^3 \text{ K}$.